Supplementary Information for

Tunable localized surface plasmon-enabled broadband light harvesting enhancement for high-efficiency panchromatic dye-sensitized solar cells

XIANGNAN DANG[1,2†], JIFA QI[1,2†], MATTHEW T. KLUG[2,3], PO-YEN CHEN[2,4], DONG SOO YUN[2], NICHOLAS X. FANG[3], PAULA T. HAMMOND[2,4*], AND ANGELA M. BELCHER[1,2,5*]

[1]Department of Materials Science and Engineering, Massachusetts Institute of Technology, Cambridge, Massachusetts 02139, USA

[2]The David H. Koch Institute for Integrative Cancer Research, Massachusetts Institute of Technology, Cambridge, Massachusetts 02139, USA

[3]Department of Mechanical Engineering, Massachusetts Institute of Technology, Cambridge, Massachusetts 02139, USA

[4]Department of Chemical Engineering, Massachusetts Institute of Technology, Cambridge, Massachusetts 02139, USA

[5]Department of Biological Engineering, Massachusetts Institute of Technology, Cambridge, Massachusetts 02139, USA

† These authors contributed equally to this work

* Correspondence should be addressed to: hammond@mit.edu, belcher@mit.edu

Supplementary discussion

Light harvesting and achievable J_{SC} (short-circuit current-density).

Light harvesting (LH), the process of capturing solar energy with electrons, is an important factor of PCE and is directly determined by the bandgap energy (E_g) and extinction coefficient (ε) of the materials. LH efficiency (LHE) limits the achievable short-circuit current density (J_{SC}) and PCE of photovoltaic devices[1] (figure S1).

Light harvesting in high- and low-absorption wavelength regions.

LH materials with low ε or non-ideal E_g inefficiently exploit the solar spectrum (usually red to near-infrared (NIR) region, figure 1c); ε is inevitably small (figure 1a,b) when the photon energy is close to E_g or faraway from Δ_gHOMO-LUMO (highest occupied molecular orbital to lowest unoccupied molecular orbital gap).

Absorption length.

The absorption length at a wavelength of λ is the reciprocal of the absorption coefficient. For a photo-absorbing layer with thickness of the absorption length, the absorbance is 1 and 90% of the light is absorbed.

The importance of balancing LH at different wavelengths and carrier collection.

Previous studies discussed the importance of balancing LH and carrier collection. However, in most cases, only the LH at λ_{Hi} is balanced with carrier collection, giving an optimized thickness of photo-absorbing layer. In fact, LH at λ_{Lo} and carrier collection is

not balanced and a thicker photo-absorbing layer is required for the balance. In this thicker film, only a small portion contributes to the LH at λ_{Hi}. As a result, only balanced LH at λ_{Hi} and λ_{Lo} can truly optimize the LH and carrier collection.

Deriving the enhancement factor.

In order to arrive at an enhancement factor, the electric-field intensity of the enhanced near field was integrated by fixing the core-shell outer radius (R_{SC}) as the characteristic length scale and considering the field contained within a two diameter sphere (indicated by the cyan circles plotted in figure 2c,S15,S17) and then divided by the EM field of the incident light over this same volume when the NP is absent. While the NP is present, the EM intensity inside the NP is considered to be zero, because no dye-molecules can access this space. The EM intensity of the rest of the space in the two diameter sphere is calculated from the FDTD simulation. In summary, $\text{Enhancement Factor}(\lambda) = \frac{|E|^2_{\text{int}}}{|E_0|^2_{\text{int}}}(\lambda) = \int_0^{2\pi}\int_0^{\pi}\int_0^{2R_{\text{CS}}} \frac{|E(r,\theta,\phi,\lambda)|^2}{|E_0(r,\theta,\phi,\lambda)|^2} r^2 \sin\theta \mathrm{d}r\mathrm{d}\theta\mathrm{d}\phi,\ |E(r,\theta,\phi,\lambda)|^2 = 0 \text{ when } 0 \le r \le R_{\text{CS}}$.

Enhancement factors in the figures of the manuscript and supplementary information.

There are overall four different ways illustrating the enhancement factors in figure 2f,g,S9,S10, which are calculated at specific wavelengths or integrated in specific wavelength regions.

The enhancement factors in figure S9 are calculated at λ_{LSPR} for TAuT NPs with d_{core}=15 nm, d_{Au}=2-6 nm and d_T=2-6 nm, and AuT and AgT with d_{core}=15 nm and d_T=2-6 nm. In

fact, since each TAuT NP with different gold and TiO_2 shell thicknesses has different λ_{LSPR}, the enhancement factor at each pixel in this figure is evaluated at a different wavelength, which is partially responsible for the discontinuity observed in the figure. The values on the color scale represent the absolute enhancement factors.

The enhancement factors of figure 2f are calculated by integrating the enhancement spectrum over 300-900 nm (400 wavelengths between 300-900 nm are calculated). The values on the color scale have arbitrary units.

The enhancement factors shown in the top part of figure 2g are calculated at different wavelengths for TAuT NPs with d_{core}=15 nm, d_{Au}=2-6 nm and d_T=2-6 nm, and AuT and AgT with d_{core}=15 nm and d_T=2-6 nm. The values on the color scale represent the absolute enhancement factors. In the bottom part of figure 2g, the enhancement factors at different wavelengths are multiplied by the normalized optical absorption of N719 and integrated over 300-900 nm (400 wavelengths between 300-900 nm are calculated). The values on the color scale also have arbitrary units. Similarly, in figure S10, the enhancement of overall dye absorption is calculated for TAuT NPs with d_{core}=15 nm, d_{Au}=2-6 nm and d_T=2-6 nm, and AuT and AgT with d_{core}=15 nm and d_T=2-6 nm.

As described in the manuscript, both the enhancement factors in figure 2f and figure S9 arise from the intrinsic ability of plasmonic NPs to enhance the near field at their characteristic λ_{LSPR} (figure S9) and in the entire vis-NIR spectrum (figure 2f). However, the enhancement factors in figure 2g and figure S10 take the surrounding photo-absorbing dyes into account. The calculated enhancement factors at different

wavelengths describe the ability to enhance the photo-absorption of N719 in both strongly-absorbeing and weakly-absorbing regions of the spectrum (the top part of figure 2g). The electric field enhancement weighted with the normalized N719 absorption spectrum and integrated over wavelengths between 300 and 900 nm represents the ability of the plasmonic NPs to enhance the overall LH of N719 (the bottom part of figure 2g and figure S10).

Maximum enhancement for TAuT NPs occurs at d_{Au}~3 nm.

In a nanoshell-like gold structure, the enhancement factor at λ_{LSPR} shows an optimum d_{Au}, which is in agreement with other literature. Xu[2] concluded that, for thin metal shells, the damping due to electron-surface collisions broadens the surface plasmon resonance peak and decreases the field enhancement. However, thick metal shells experience increased absorption, which also diminishes the field enhancement. Tanabe[3] calculated the enhancement around nanoparticles and dielectric-metal core-shell structures within the quasistatic limit (i.e. $R_{CS}<<\lambda$) and also saw that the dielectric-metal core-shells had a significantly higher field enhancement compared to metal-dielectric core-shells. They also noticed that an optimum core-shell ratio of (R_{core}/R_{CS})~0.9 maximized enhancement. For this work, it is maximized at a value of ~0.73.

Different λ_{LSPR} achieved from simulations and experiments (solution of NPs).

The λ_{LSPR} achieved from simulations and experiments (solution of NPs) are slightly different, because in the simulation the parameters from crystalline TiO_2 are used, which is different from the amorphous TiO_2 coatings for the (multiple-)core-shell NPs as

synthesized in solution, but similar to the crystalized TiO_2 coating (anatase) after annealing at 500°C in the DSSCs. Therefore, although there is a slight difference between the simulation results and the absorption spectra of the solutions, the simulated results are close to the condition used in the actual devices.

Ease of tunability of λ_{LSPR} for TAuT NPs compared to other geometries of plasmonic NPs.

Little change in synthesis is required to tune the λ_{LSPR} of TAuT NPs due to their high sensitivity to geometry. For a 15 nm in diameter TiO_2 core, tuning the gold shell thickness from about 1 nm to 4 nm experimentally achieved λ_{LSPR} of 1000-600 nm, which is realized by simply adding different amounts of gold precursor (or reducing agent). However, for gold nanorods[4], tuning the λ_{LSPR} from 550 nm to 800 nm requires the aspect ratio of the nanorods changing from 1 to 4, which involves more sophisticated synthesis and more geometric modification than simply changing the gold shell thicknesses in the TAuT NPs. Moreover, for Au nanoplates with cylindrical or triangular shapes, the synthesis is even more complicated and is difficult to control[5].

Simulated absorption spectra of N719 enhanced by plasmonic NPs with λ_{LSPR} from 400 to 700 nm.

The simulated absorption spectra of N719 enhanced by plasmonic NPs with different λ_{LSPR} were obtained by multiplying (normalized) absorption spectrum of N719 and the enhancement factors (as a function of wavelength) at each wavelength (the left part of figure S11). The enhancement factors (as a function of wavelength) are represented by

the Gaussian distributions with center at 400-700 nm and full-width at half-maximum (FWHM) about 100 nm (the right part of figure S11). The maximum enhancement factors of 2 are considered, and the enhancement factors away from λ_{LSPR} are set to 1, *i.e.* $\text{Enhancement Factor}(\lambda) = \mathrm{e}^{\frac{-(\lambda-\lambda_{\mathrm{LSPR}})^2}{2000}} + 1, \text{where } \lambda_{\mathrm{LSPR}} = 400 - 700 \text{ nm}.$

Calculation of the concentrations of plasmonic NPs.

For all of TiO_2 (3.9 g cm^{-3} of density), Ag (10.5 g cm^{-3} of density), and Au (19.3 g cm^{-3} of density) core NPs, the particle concentrations were estimated by assuming that (1) the reactions went to completion for the synthesis of core particles and (2) the NP batch was monodispersed with a uniform distribution of ~15 nm particles in diameter. An estimated yield of 80% was used when considering the loss during washing and centrifugation steps after the NPs were coated to form TAuT, AgT, and AuT (multiple-)core-shell NPs.

The plasmonic AgT NPs-TiO_2 ratios in the photoanodes are from 0.01-1.0 wt%, which corresponds to a volume density of 0.003-0.3 vl% and a particle density of 8.4×10^{12}-8.4×10^{14} cm^{-3}, assuming that the porosity of TiO_2 photoanodes is 0.60, as demonstrated in the literature using the same composition of TiO_2 paste[1] (including 9 wt% ethyl cellulose as binders and 73 wt% terpineol as solvent).

The total number of NPs is calculated by: $\text{total \# of NPs} = \frac{\text{total \# of moles}}{\text{\#of mole per NP}} = \frac{\text{concentration} \times \text{volume}}{\left(\frac{4}{3}\right)\pi r^3 \times \frac{\rho}{M_{\mathrm{w}}}}$. In the above equation, *r* is the radius of the NP, ρ is the density, and M_{w} is the atomic weight.

Subsequently, for AuT and TAuT NPs, the ranges of plasmonic particle densities in TiO_2 photoanodes are chosen to be the same as AgT-incorporated photoanodes. Considering the different densities of Ag, Au, and TAu NPs, the Au-TiO_2 and TAu-TiO_2 ratios in the photoanodes are 0.018-1.8 wt% and 0.032-3.2 wt%, respectively. For the volume density, AuT NPs have the same range with AgT NPs; considering a TAuT NP with d_{Au}=3 nm and d_T=2 nm, the volume density of TAuT NPs in the photoanode is 0.0069-0.69 vl%. There exists a factor of 2 to 3 comparing the volume densities of TAuT and AgT or AuT NPs, due to the different core radius and shell thickness. We believe that this is not responsible for the different device performance we observed, simply because, even for the same concentration of different plasmonic NPs, the different device performance still exists.

The possible reasons for V_{OC} enhancement induced by plasmonic NPs-incorporation.

1. The relationship between V_{OC} and the thickness of the photoanode shows that V_{OC} increases with decreasing the thickness of photoanodes, which is due to less charge recombination. Since the plasmon-enhanced DSSCs feature thinner photoanodes for optimized PCE due to the enhanced LH ability, the V_{OC} of the optimized plasmon-enhanced DSSC is thus larger than the V_{OC} of the optimized DSSCs without plasmonic NPs.

2. In terms of the material properties of electronic structure, the V_{OC} of a DSSC is determined by the difference between the quasi-Fermi level of TiO_2 and the redox potential of electrolyte. By introducing plasmonic NPs, the quasi-Fermi level is lifted due

to the equilibrium between quasi-Fermi level of TiO_2 and LSP energy level of plasmonic NPs[6, 7]. The ground states of the electrons in plasmonic NPs are the Fermi level, and the work functions for Ag and Au are 4.7 eV and 5.1 eV, respectively. Considering that the energy difference between the ground state and the surface plasmon state of the electrons is provided by the photo-excitation, this energy difference is 3.0 eV, 2.3 eV, and 1.8 eV, corresponding to 420 nm, 550 nm, and 700 nm of λ_{LSPR} for AgT, AuT, and TAuT NPs, respectively. Therefore, AgT, AuT, and TAuT NPs have the highest to lowest LSP energy levels, which could be responsible for that the TAuT NPs increase V_{OC} less significantly than AgT and AuT NPs. In addition, the different interfaces of metal-TiO_2 and different recombination rates induced by metal particles (non-ideal outer TiO_2 coating exists) could also be related to the different V_{OC} enhancement.

Comparing simulated and experimental results of dye LH enhancement at λ_{LSPR}.

The simulated enhancement factor of TAuT NPs with d_{core}=15 nm, d_{Au}=3 nm and d_T=2 nm gives a maximum value of 7.2. As described previously, this enhancement factor is obtained by integrating in a region 8 times the volume of the NP (volume density 12.5%). We assume that the EM intensity is not significantly enhanced by the LSP in the space beyond the two-diameter spherical cutoff. In this case, we can use the above-calculated volume densities of plasmonic NPs to arrive at another enhancement factor, which considers the exact volume density of plasmonic NPs in the photoanodes. The calculated enhancement factor for TAuT NPs with a volume density of 0.69 vl% would be

1.4. Comparing to the enhancement factor obtained from optical absorption spectra (figure 2h), the simulation and experimental results are comparable.

Correlation of the optical density, light harvesting efficiency, and IPCE.

It is worth noting that the optical density (OD), LHE, and IPCE are all correlated. LHE relates to OD as LHE(λ)=1-Transmittance(λ)=1-$10^{-OD(\lambda)}$. The LHE enhancement is achieved as, $\Delta LHE(\lambda)/LHE_0(\lambda)=(LHE_{LSP}(\lambda)-LHE_0(\lambda))/LHE_0(\lambda)=(1-10^{-OD(\lambda),LSP})/(1-10^{-OD(\lambda),0})-1$. Considering IPCE($\lambda$)=LHE($\lambda$)CSE($\lambda$)CCE($\lambda$) (CSE is charge separation efficiency, CCE is charge collection efficiency) and CSE and CCE are not affected by LSP as strongly as LHE is, $\Delta IPCE(\lambda)/IPCE_0(\lambda)\approx\Delta LHE(\lambda)/LHE_0(\lambda)$. In fact, the experimental results of OD and IPCE enhancement are in agreement, which indicates that the IPCE improvement mainly arises from LSP-enhanced LHE.

For an optically-thin photoanode, assuming an OD of 0.2 at λ_{max}, the light harvested is 1-$10^{-0.2}$=36.9%, neglecting reflection by the glass substrate and photo-absorption by the electrolyte. Considering the plasmonic NPs enhance the OD by 100% (to OD=0.4), the improved light harvesting efficiency is 1-$10^{-0.4}$=60.2%, improved by 63%. For an optically-thick photoanode, assuming an OD of 1 at λ_{max}, the light harvesting efficiency is 90%. If the OD is also enhanced by 100% (to OD=2), the light harvesting efficiency would be 99%, improved only by 10%. Similar to the discussion in the manuscript, for optically-think photoanodes, the impact of enhancing the photo-absorption in the strong-absorption range of dye-molecules is small, while great enhancement can be achieved by improving the photo-absorption in the weak-absorption range of dye-molecules.

Difference of IPCE at λ_{max} for optically-thick films.

All AgT, AuT, and TAuT NPs improve the IPCE of optically-thick photoanodes at λ_{max} by less than 5%. There are several possible reasons. IPCE(λ)=LHE(λ)CSE(λ)CCE(λ). Due to the reason described in the manuscript, for TiO_2-only photoanodes or plasmonic NPs incorporated-photoanodes, the LHE at λ_{Hi} (especially λ_{max}) and CCE should be balanced and are close to unity. However, slight difference still exists for the LHE and CCE due to the thinner photoanodes for optimized PCE for the following reasons. First, even for the photoanodes with the same optical density, thinner photoanodes would have less loss of incident light due to the optical absorption from electrolyte (*e.g.*, iodine in the electrolyte absorbs visible light). Second, thinner photoanodes have higher CCE due to similar electron diffusion length. In addition, it is possible that the CSE is affected by plasmonic NPs, due to the changed photo-physical processes, *e.g.* increased radiative recombination rate has been observed as enhancement of photoluminescence. Consequently, the IPCEs at λ_{max} of plasmonic NPs-incorporated optically-thick photoanodes are improved slightly.

The effect of plasmonic NPs on fill factors.

There is no significant decreasing or increasing effect of the plasmonic NPs on the fill factors of the DSSCs. However, compared to a small variation of the fill factors of TiO_2-only DSSCs, the fill factors of the DSSCs with plasmonic NPs show a similar average but a larger variation. This is probably due to the preparation of plasmonic NPs-incorporated TiO_2 paste. Since we prepared the TiO_2 pastes for each condition (each type of NPs, each

concentration, and for doctor-blading and spin-coating) in a relatively small amount, the quality of the plasmonic NPs-incorporated pastes is not as perfect as the original TiO_2 paste, which is prepared in a relatively large amount. The large variation in fill factor is also responsible for the variation observed for the PCEs. However, we believe that, if the plasmonic NPs-incorporated TiO_2 pastes are prepared in large quantity, this issue could be easily solved.

Higher concentrations of plasmonic NPs decrease the device performance.

As shown in many previous publications[7, 8], higher concentrations of plasmonic NPs would decrease the device performance due to both saturated effect of LSP-enhancement and increasing defects and impurities incorporated by the plasmonic NPs. In our experiments, although we did not observe obvious decrease using high concentrations of plasmonic NPs, the device performances of the highest and the second highest concentrations of plasmonic NPs are similar, which indicates that the saturation point has been reached at this concentration range.

Supplementary Materials and Methods

Materials.

Sodium citrate, silver nitrate ($AgNO_3$), tetra chloroauric acid ($HAuCl_4$), acetic acid, hydroxylamine (NH_2OH), titanium tetrachloride ($TiCl_4$), ethyl cellulose, terpineol, acetonitrile, turt-butanol, 1-butyl-3-methylimidazolium iodide, iodine, guanidinium thiocyanate, 4-tert-butyl pyridine, and valeronitrile are purchased from Sigma Aldrich. Titanium isopropoxide (TPO, 97%), Titanium butoxide (TBO, 98%), polyvinylpyrrolidone with an average molecular weight of 8,000 (PVP-8) and poly (allylamine hydrochloride) (PAH) were purchased from Alfa; ethanol (99.5%), acetone (99.5%), nitric acid (70%), and ethylene glycol (99.9%) were purchased from Mallinckrodt Chemicals; ammonia (28-30 wt% NH_3 in water) was purchase from VWR International Inc. Poly(acrylic acid) (PAA, average molecular weight 5,000, 50% aqueous solution) was obtained from Polysciences, Inc. Cis-diisothiocyanato-bis(2,2'-bipyridyl-4,4'-dicarboxylato) ruthenium(II) bis(tetrabutylammonium) (also named N719 or Ruthenizer 535-bisTBA, purchased from Solaronix) was used as a 0.5 mM solution in acetonitrile and tert-butanol (volume ratio = 1:1). All chemicals were used as received. All water was deionized (18.2 MΩ, milli-Q pore).

Synthesis of AgT NPs.

The Ag NPs of an average diameter of 15 nm were synthesized by a modified polyol process and described in previous publication[8]. Typically, 0.1 mmol of silver nitrate was added into 25 ml of ethylene glycol solution containing 0.5 g of PVP-8 and the mixture

was kept stirring at room temperature until silver nitrate was completely dissolved. Then the solution was slowly heated up to 120°C and kept at the temperature for 1 hour with constant stirring. After the reaction, 12.5 ml of the as synthesized Ag NPs in ethylene glycol (containing 0.05 mmol of Ag) was added with 5 ml of 1% PAA aqueous solution. The solution was kept stirring for over 4 hours and then added with 100 ml of acetone and centrifuged at 3,000 r.p.m. Then the supernatant was removed and the Ag NPs were washed again with ethanol, and centrifuged at 10,000 r.p.m.

The Ag NPs were then redispersed in 25 ml of ethanol. After cooling down the solution with ethylene glycol-dry ice bath, 1 ml of ethanol solution containing 10 µl of TBO was added into the solution. The reaction was kept stirring in the dark for 1 hour, and then sonicated in a bath sonicator for 30 minutes, after which the reaction was kept stirring in the dark for a certain time to achieve requested TiO_2 shell thickness (typically 12 hours).

Synthesis of AuT NPs.

100 ml of 0.01% $HAuCl_4$ solution in a 300 ml round-bottom flask was heated to boiling with vigorous stirring. 1.8 ml of 1 wt% sodium citrate aqueous solution was added to the reaction. The solution color turned to blue within 25 seconds; and to red-violet 70 seconds later. The reaction was kept on boiling for another 30 minutes; then the solution was stirred for another 15 minutes while the heating source was removed. TEM image indicated an average diameter of 15 nm for the Au NPs. To the as-synthesized solution, 5 ml of 5% PVP aqueous solution was added and kept stirring for 12 hours.

Then, after centrifuging at 18,000 r.p.m., the supernatant was removed and the Au NPs were washed with ethanol and centrifuged again.

The Au NPs were redispersed into 25 ml of ethanol and used for the synthesis of AuT core-shell structure. After cooling down the solution with ethylene glycol-dry ice bath, 1 ml of ethanol solution containing 10 µl of TBO was added into the solution. The reaction was kept stirring in the dark for 1 hour, and then sonicated in a bath sonicator for 30 min, after which the reaction was kept stirring in the dark for a certain time to achieve requested TiO_2 shell thickness (typically 12 hours).

Synthesis of TiO_2 NPs.

The 15-20 nm sized TiO_2 nanocrystals were synthesized using the procedure in the literature[9]. An amount of 1.2 g (0.02 mol) of acetic acid was added all at once to 5.86 g (0.02 mol) of TPO under stirring at room temperature. The modified precursor was stirred for about 15 minutes and poured into 29 ml water as quickly as possible while vigorously stirring (700 r.p.m.). A white precipitate was instantaneously formed. One hour of stirring was required to achieve a complete hydrolysis reaction. After adding a quantity of 0.4 ml of 70% nitric acid, the mixture was heated from room temperature to 80°C within 40 minutes and kept at the temperature for another 75 minutes. Water was then added to the cooling liquid mixture to adjust the volume to a final 37 ml. The resultant mixture was kept in a 57 ml Teflon-lined autoclave and heated at 250°C for 12 hours. Following this step, 0.24 ml of 70% nitric acid was added and the dispersion was sonicated to re-disperse in water.

Synthesis of TAuT NPs.

The as-synthesized TiO_2 NPs were dispersed in DI water and were positively charged because of the H^+ termination. The surface of the NPs was modified by layer-by-layer (LbL) coating of polyelectrolytes[10-13] (zeta-potentials of the polyelectrolytes-coated NPs are shown in figure S3). To the 50 ml of 5 mM TiO_2 NPs aqueous solution, 10 ml of 5% PAA solution was added in order to modify the NPs with a negatively charged polyelectrolyte and incubated for 6 hours at room temperature with stirring. The dispersion was then precipitated by centrifugation at 12,000 r.p.m. and redispersed in DI water (repeated three times) to remove excess PAA. To modify the NPs with a positively charged polyelectrolyte layer, to PAA-coated NPs aqueous solution, 10 ml of 5% PAH aqueous solution was added and incubated for 12 hours at room temperature with stirring. The NPs were then centrifuged and redispersed in DI water to remove excess polyelectrolyte (repeated three times). Sequentially, another PAA and PAH layers were coated by repeating incubation, precipitation and dispersion in DI water. LbL modified NPs were characterized by zeta-potential measurements. 50 ml of the aforementioned solution containing 100 μmol TiO_2 and 3 ml of 1% $HAuCl_4$ were mixed and diluted with DI water to 100 ml. The $HAuCl_4$ precursor was incubated with the PAA/PAH/PAA/PAH coated particles for more than 6 hours for complexation and immobilization on the particle surface at room temperature. Then, the flask of solution was immersed in acetone-iced water bath and the solution was allowed to cool down. Subsequently, 5% hydroxylamine aqueous solution was added dropwise to initiate the surface confined

growth of the gold-shell. After the reaction, 10 ml of 5% PAA aqueous solution was added into the solution and incubated for more than 4 hours.

The gold-shell encapsulated particles TAu were obtained, and were centrifuged, washed and redispersed in 25 ml of ethanol for coating TiO_2 outer shell. After cooling down the solution with ethylene glycol-dry ice bath, 1 ml of ethanol solution containing 10 µl of TBO was added into the solution. The reaction was kept stirring in the dark for 1 hour, and then sonicated in a bath sonicator for 30 minutes, after which the reaction was kept stirring in the dark for a certain time to achieve requested TiO_2 shell thickness (typically 12 hours).

Other geometries of plasmonic NPs.

The silver nanocubes and gold nanocages are synthesized using previously published method[14, 15]. The gold nanorods (10 nm in diameter and different aspect ratios to achieve λ_{LSPR} between 700 to 800 nm) are purchased from Strem Chemicals, Inc.

TEM Characterization of plasmonic NPs.

TEM observations of the synthesized nanostructures (TiO_2, Ag, Au, AgT, AuT, TAu, and TAuT) were performed using JEOL 2010, JEOL 2010F, and JEOL 2100F TEMs with an accelerating voltage of 200 kV. TEM samples were prepared by directly dropping nanoparticle solutions to carbon supported copper or nickel grids. To get better contrast image, the high contrast objective aperture was used for all images. The high resolution image was taken under smaller illumination area size by changing the alpha selector.

The STEM images were taken by both Gatan High-Angle Annular Dark Field (HAADF) and Bright filed (BF) detectors under 0.2 nm probe size and 12 cm camera length.

Zeta-potential measurement of alternating polymer PAA and PAH-coated TiO_2.

Zeta-potential were measured at an accumulation time of 10 with 5 measurements per sample at 20 V using DelsaNano (Beckman Coulter). Electrophoretic mobility was calculated using the Smoluchowski approximation.

Thermal stability of the plasmonic NPs characterized by TEM.

For the thermal stability observation, the grids with nanoparticles were heated at 450 to 500°C for 15 to 30 minutes in argon atmosphere and followed by fast quenching.

Optical absorption measurement of the solutions of plasmonic NPs

For both solutions and thin films of AgT, AuT, and TAuT NPs, the optical absorption measurements were performed using a Beckman Coulter DU800 UV-Vis spectrophotometer.

Optical absorption enhancement of dye-molecules induced by the incorporation of plasmonic NPs.

3-μm-thick thin films of TiO_2 NPs or TiO_2 NPs incorporated with plasmonic NPs on 2.5x2.5 cm^2 fused silica wafers were used for thin-film optical absorption measurements, which were prepared by spin coating (Specialty Coating Systems, 6800 spin coater) and followed by annealing treatment at 500°C for 15 minutes. Then the film thickness was

measured using a Dektak 150 surface profiler. These films were immersed into 0.1 mM ruthenium dye solution (volume ratio of acetonitrile to tert-butanol is 1:1) and kept at room temperature for 12 hours. Then the dyed films were immersed in acetonitrile for 5 min to remove non-adsorbed dye molecules. 3-μm-thick films were used because of the small interference and scattering effects in the optical absorption spectroscopy observations at this thickness. The absorbance shown in figure 2h is the absorbance of N719-sensitized different plasmonic NPs-incorporated TiO_2 films subtracted by the absorbance of the TiO_2 films, which describes the absorption of the dye-molecules.

Thermal stability of the plasmonic NPs characterized by optical absorption.

Plasmonic NP solutions (AgT, AuT, TAuT, and Au nanocage@TiO_2) were directly drop-casted on the glass slides to form thin films. The thin films were dried at a temperature from room temperature to 80^{o}C. After these thin films were annealed at 500°C for 30 minutes in air, the optical absorption measurements for these thin films were performed using a Beckman Coulter DU800 UV-Vis spectrophotometer.

Synthesis, optical characterization, and thermal stability of other geometries of plasmonic NPs with tunable λ_{LSPR} in vis-NIR region.

Different geometries of plasmonic nanomaterials (gold nanorods, gold nanodisks, and gold hollow shells) were purchased or synthesized using previously published methods. They were coated with TiO_2 thin shells using the same method for coating Ag, Au, and TAu NPs. The TEM and optical characterization for the thermal stability of these

geometries of plasmonic nanomaterials were also carried out using the same method for AgT, AuT, and TAuT NPs.

FDTD simulation of AgT, AuT, TAuT, and other geometries of plasmonic NPs.

The near-field response of core-shell structures to a plane-wave excitation was evaluated with the finite-difference time-domain (FDTD) method using the software Lumerical FDTD Solutions Version 8.0.0. The two core-shell geometries considered in this paper are (1) a silver or gold spherical nanoparticle with a thin TiO_2 coating (i.e. AgT and AuT) and (2) a spherical TiO_2 nanoparticle with a thin gold coating that is further cladded in an outer TiO_2 coating (i.e. TAuT). Each core-shell type was modeled as a set of two or three concentric spheres, respectively, and was placed in an ethanolic environment with refractive index 1.36 and illuminated by a plane wave. All of the simulations performed modeled the core, regardless of material, as a 15 nm diameter sphere (unless otherwise specified). The shell thicknesses were varied between 2 and 6 nm by increments of 0.2 nm. All simulations were performed with a mesh size of 1 nm and the conformal meshing option “Conformal variant 1” was applied to provide greater accuracy, particularly at the metal-TiO_2 interfaces[16]. Each core-shell geometry was subjected to a plane-wave illumination at 400 different wavelengths between 300 and 900 nm. A fourth order polynomial was fitted over this wavelength range to the measured dielectric data of silver and gold as reported by Palik[17]. The refractive index of TiO_2 was approximated as 2.34 and taken to be constant over the wavelengths of

interest. This value was found by averaging the dispersion relation reported by Kim[18] between the wavelengths of 350 and 950 nm.

In order to generate an enhancement factor that evaluates the nanoparticle's ability to concentrate light in the near-field zone, the total electric field intensity was integrated over the space between the outermost core-shell surface and a fictitious sphere locate one core-shell radius away and divided by the integral of the incident plane wave's electric field intensity over the entire volume enclosed by the fictitious sphere, including the nanoparticle volume. This definition is meant to compare the amount of electric energy contained in the near-field surrounding the particle (where the dye molecules are present in the DSSC) to the amount of energy available to the same region under the plane-wave illumination in the absence of the particle.

$$\text{Enhancement Factor}(\lambda) = \frac{|E|^2_{\text{int}}}{|E_0|^2_{\text{int}}}(\lambda) = \frac{\int_0^{2\pi}\int_0^{\pi}\int_{R_{\text{cs}}}^{2R_{\text{cs}}}|E(r,\theta,\phi,\lambda)|^2\, r^2 \sin\theta \,\mathrm{d}r\mathrm{d}\theta\mathrm{d}\phi}{\int_0^{2\pi}\int_0^{\pi}\int_0^{2R_{\text{cs}}}|E_0(r,\theta,\phi,\lambda)|^2\, r^2 \sin\theta \,\mathrm{d}r\mathrm{d}\theta\mathrm{d}\phi}$$

where R_{CS} is the outer radius of the core-shell particle, E is the total electric field in the near-field, and E_0 is the electric field of the incident plane wave.

Preparation of TiO_2 paste for spin-coating and doctor-blading.

Two kinds of pure ethyl cellulose (EC) powders, i.e., EC (5–15 mPas) and EC (30–50 mPas) were dissolved prior to usage in ethanol to yield 10 wt% solutions. 4.5 g of EC (5–15) and 3.5 g of EC (30–50) of these 10 wt% ethanol solutions were added to a round bottom flask containing 1.6 g pure TiO_2 (obtained from previously prepared precipitate)

and 6.5 g of terpineol and diluted with 8 ml of ethanol to obtain a final total volume of 28 ml. This mixture was then sonicated using an ultrasonic horn. Ethanol and water were removed from these TiO_2/ethyl cellulose solutions by rotary-evaporator. The final doctor-blading pastes correspond to 18 wt% TiO_2, 9 wt % ethyl cellulose and 73 wt % terpineol. For each doctor-blading process using the scotch-tape, a film of 5-7 μm was formed.

To achieve the spin-coating paste, the doctor blading paste was diluted by terpineol 2 to 3 times. By adjusting the spin-coating speed from 1000 to 3000 r.p.m., the film thicknesses from 3 to 1 μm were obtained.

Fabrication of photoanodes of DSSCs.

The FTO glass (TEC15 2.2 mm thickness, 15 $\Omega\ \square^{-1}$, Pilkington, USA) was first cleaned in a detergent solution using an ultrasonic bath for 15 minutes, and then rinsed with water and ethanol. After treatment in an air plasma system for 1 minute, the FTO glass plates were immersed into a 40 mM of aqueous $TiCl_4$ solution at 80°C for 30 minutes and washed with water and ethanol. The fabrication of the 1-4 μm thick photoanodes of both TiO_2-only DSSCs and plasmon-enhanced DSSCs was performed by spin coating (for one or two times), the same method used for preparing the thin films for optical absorption measurement. For DSSCs with a photoanode thickness larger than 5 μm, the fabrication was carried out using the doctor-blading procedure. A layer of paste was coated on the FTO glass plates by doctor blading, left for 3 minutes to reduce the surface irregularity of the paste, and then dried for 5 minutes at 120°C. This doctor

blading procedure with paste (coating, storing, and drying) was repeated to get an appropriate thickness about 5-20 μm for the photoanodes. The film thickness was measured using a Dektak 150 surface profiler. The photoanodes were sintered at 500°C for 30 minutes after the required thicknesses of photoanodes were achieved. The TiO_2 films were then treated with 40 mM of $TiCl_4$ solution at 80°C for 30 minutes again, rinsed with water and ethanol, and then sintered again at 500°C for 30 minutes. After cooling to 80°C, the TiO_2 electrodes were immersed into a 0.5 mM of N719 dye in a mixture of acetonitrile and tert-butyl alcohol (volume ratio, 1:1), and were kept at room temperature for 24 hours. The photoanodes incorporated with plasmonic NPs were fabricated with a modified procedure. The different amounts of AgT, AuT, and TAuT NPs in ethanol solution (plasmonic NPs to TiO_2 NPs ratio ~0.01-3.2 wt%) were mixed with the TiO_2 paste (mixture of TiO_2 NPs, ethyl celluloses, and terpineol), followed by stirring and sonicating. Then the ethanol was removed by a rotary-evaporator. After the pastes incorporated with plasmonic NPs were achieved, the fabrication procedure of the photoanodes of plasmon-enhanced DSSCs was the same as that of the TiO_2-only DSSCs.

Assembly of DSSCs with photoanodes, electrolyte, and counter electrodes.

The counter electrodes were 100-nm-thick platinum, sputtered on ITO substrates (Delta Technologies). The electrolyte was a solution of 0.6 M 1-butyl-3-methylimidazolium iodide, 0.03 M iodine, 0.10 M guanidinium thiocyanate, and 0.5 M 4-tert-butyl pyridine in a mixture of acetonitrile and valeronitrile (volume ratio, 85:15). The dye-adsorbed TiO_2 or plasmonic NPs-incorporated TiO_2 photoanodes and Pt counter electrodes were

assembled into a sandwich type cell and sealed with a hot-melt Surlyn of 25 μm in thickness (Solaronix). The size of the TiO_2 electrodes used was 0.16 cm^2 (4 mm×4 mm). The actual active areas of the devices were accurately measured by a photo scanner. The aperture of the Surlyn frame was larger than that of the TiO_2 area by 2 mm. Copper tape was adhered on the edge of the FTO outside of the cell. The position of the tape was 1 mm away from the edge of the Surlyn gasket and 4 mm away from the edge of the TiO_2 layer.

Characterization of DSSCs.

Photovoltaic measurements were performed under illumination generated by an AM 1.5 solar simulator (Photo Emission Tech.). The power of the simulated light was calibrated to 100 mW/cm^2 by using a reference Si photodiode with a powermeter (1835-C, Newport) and a reference Si solar cell in order to reduce the mismatch between the simulated light and AM 1.5. The J-V curves were obtained by applying an external bias to the solar cells and measuring the generated photocurrent with a Keithley model 2400 digital source meter. The voltage step and delay time of the photocurrent were 10 mV and 40 ms, respectively. A black tape mask was attached to the device in order to prevent irradiations from scattered light.

Spectral response of incident photon-to-current conversion efficiency (IPCE).

IPCE spectra were measured with a commercial IPCE measurement system (Model QEX7, PV Measurements, Inc.). Under full computer control, light from a xenon arc lamp (150 W) was focused through a grating monochromator, equipped with two 1200 lines/mm

diffraction gratings, onto the photovoltaic cell under test. The monochromator was incremented through the visible spectrum (from 350 nm to 850 nm) to generate the spectral response of IPCE with a spectral resolution of 10 nm. The incident photon flux was determined using a calibrated silicon photodiode (calibrated by PV Measurements, Inc.). Measurements were performed in a short-circuit condition, while the cell was under background illumination from a bias light of 50 mW/cm^2. Bias illumination was from the same direction as the monochromatic light, which was from the FTO side. The monochromatic beam was chopped using a computer-controlled shutter at a frequency of 1.33 Hz, and averaging of up to 10 shutter cycles was employed.

Electrochemical impedance spectroscopy (EIS).

Electrochemical impedance spectra measurements of DSSCs were performed with a Solartron 1260 frequency response analyzer. The spectra were measured at various forward bias voltages (from -0.85 to -0.45 V) in the frequency range of 0.1 Hz~1 MHz with oscillation potential amplitudes of 10 mV at room temperature. The photoanode was connected to the working electrode. The Pt electrode was connected to the auxiliary electrode and the reference electrode. The impedance measurements were carried out in dark conditions.

Calculation of electron diffusion length from electrochemical impedance spectra.

The electron diffusion length, L_n, can be calculated from $L_n=L(R_{REC}/R_T)^{1/2}$, where L is the film thickness, R_{REC} is electron recombination resistance, and R_T is electron transport resistance. R_{REC} and R_T were obtained by fitting the measured electrochemical

impedance spectra to the equivalent circuit (known as transmission line model, shown in Figure S20) with the Z-view software (v3.2b, Scribner Associates Inc.).The transmission line component (Z_{TiO2} in Figure S20) in an equivalent circuit is often used to represent the interface resistance and capacitance for a porous structure, which is the case for the photoanodes of DSSCs. During fitting the electrochemical impedance spectra to the transmission line model, the resistance and capacitance at the substrate/TiO_2 interface, and the substrate/electrolyte interface were assumed negligible due to good contact between the substrate, the TiO_2 NP layer, and the blocking layer of TiO_2, achieved by $TiCl_4$ treatment to the substrate. In Figure S21, electrochemical impedance spectra from each type of DSSCs, measured at 600 mV, are shown in symbols. The fitted results are shown as solid lines. For more detailed information about fitting electrochemical impedance spectra to the transmission line model and extracting electron diffusion length from fitted electrochemical impedance spectra, refer to references[19-23].

Calculation of electron collection efficiency from electron diffusion length.

The electron collection efficiency is[20], $\eta_{\mathrm{COL}} = \frac{[-L\alpha\cosh\left(\frac{d}{L}\right)+\sinh\left(\frac{d}{L}\right)+L\alpha\mathrm{e}^{-\alpha d}]L\alpha}{\left(1-\mathrm{e}^{-\alpha d}\right)[1-L^2\alpha^2]\cosh(\frac{d}{L})}$, where *d* is the thickness of the TiO_2 film, *L* is the electron diffusion length, and α is the absorption coefficient of dye-sensitized TiO_2 film. For the calculation, we assume αd equals to 1, indicating 90% of the incident light is absorbed. We observed very similar electron diffusion lengths for all types of DSSCs. Thinner photoanodes (smaller *d* and larger *L*/*d*) thus result in larger values of η_{COL}.

Supplementary Figures

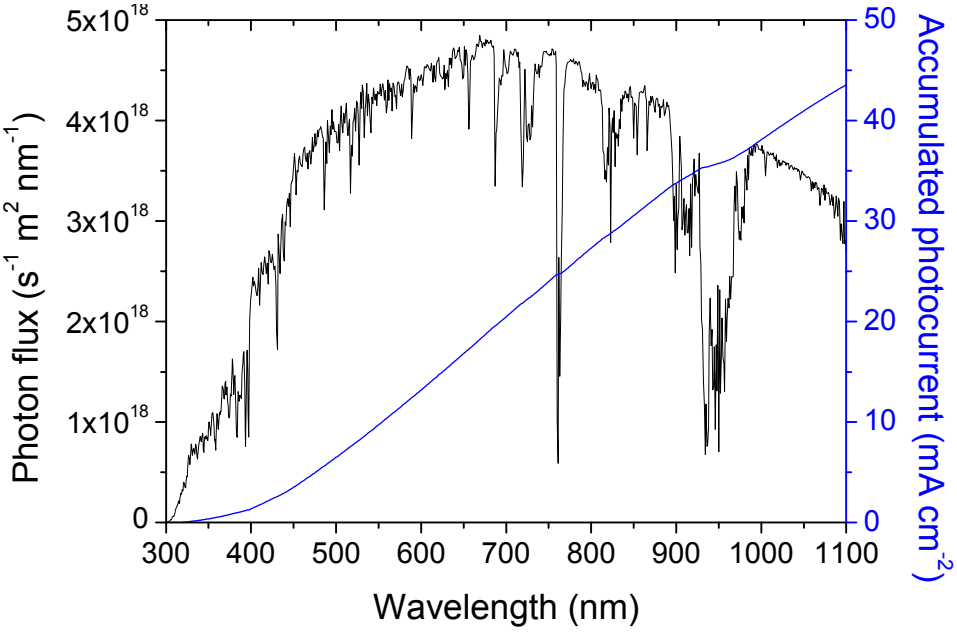

Figure S1. Light harvesting and the achievable J_{SC}. Photon flux of the AM 1.5 G spectrum at 1000 W m^{-2} (ASTM G173-03) and the calculated accumulated photocurrent (assuming 100% quantum efficiency).

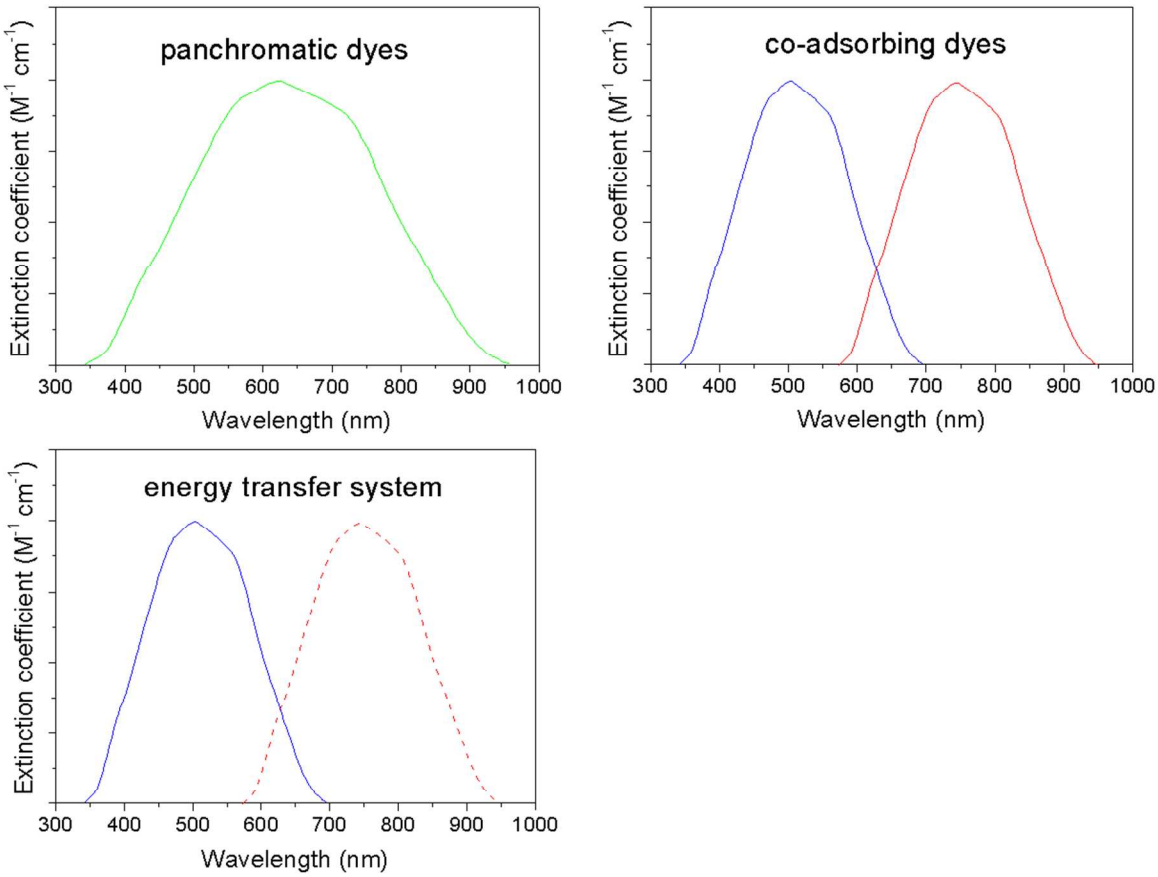

Figure S2. Illustrations for previous efforts for panchromatic DSSCs, including the development of panchromatic dyes (broadband-absorbing dye-molecules), co-adsorbing dyes (energy is absorbed by small-bandgap and large-bandgap materials together), and energy relay systems (energy absorbed by small-bandgap materials is transferred to large-bandgap materials and harvested by carrier separation and collection).

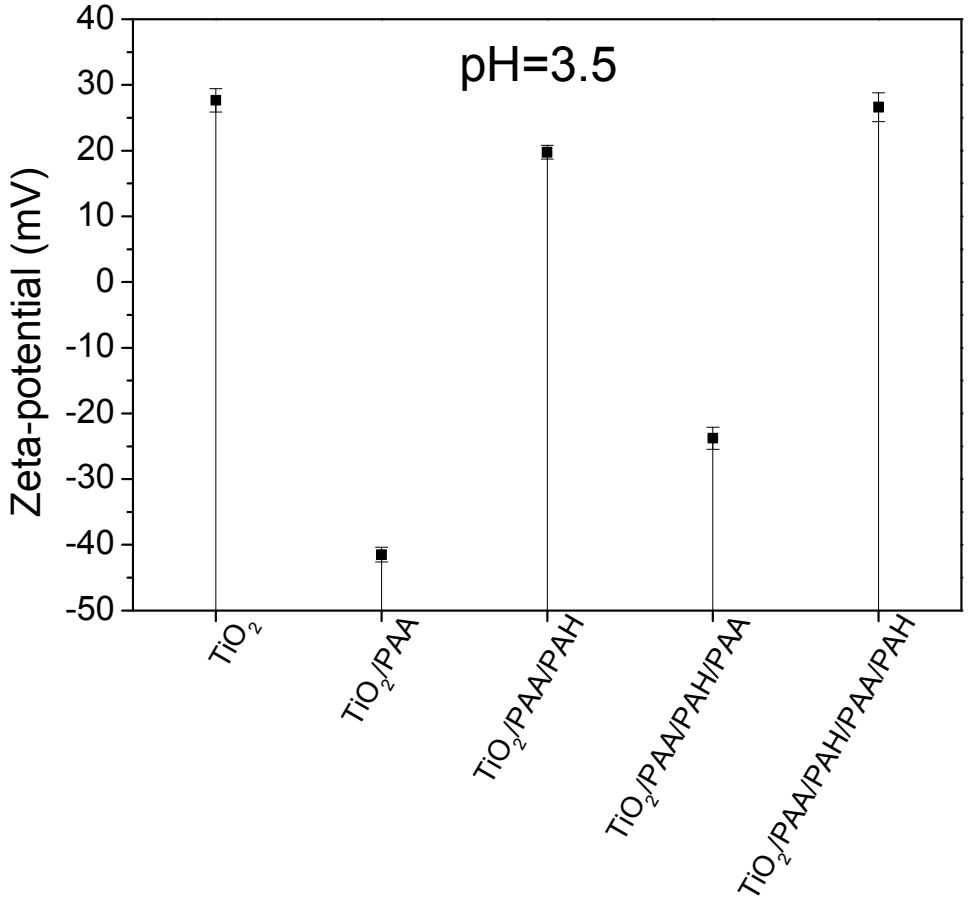

Figure S3. Zeta-potentials of alternating polymer PAA and PAH-coated TiO_2 NPs. All zeta-potentials are measured at pH=3.5.

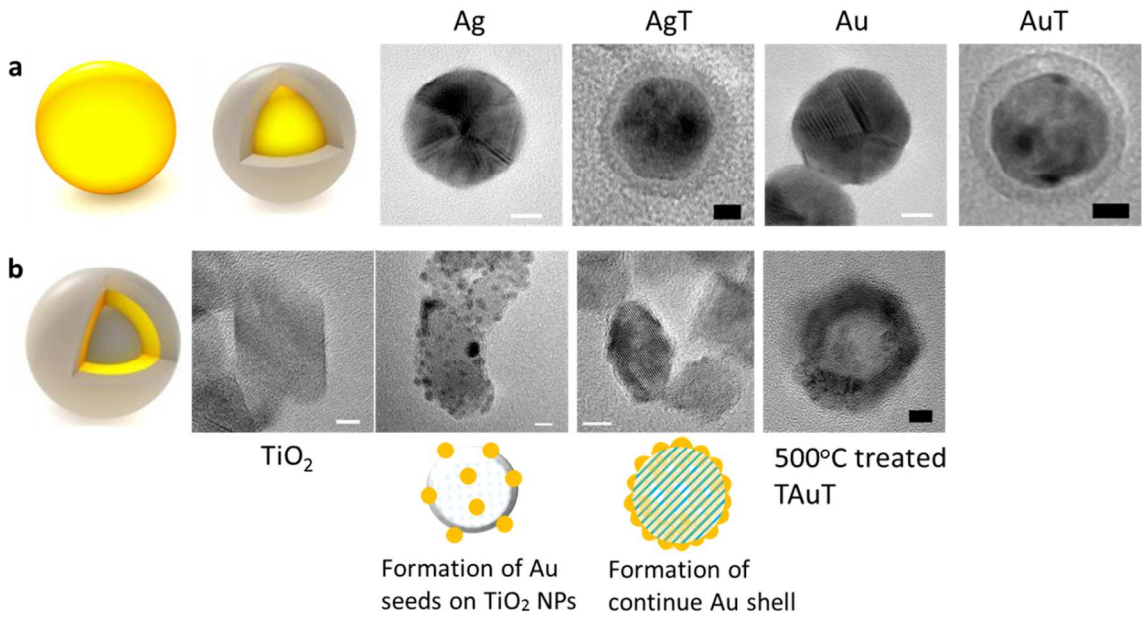

Figure S4. Synthesis of core-shell AgT and AuT and multiple-core-shell TAuT NPs. a, illustrations and transmission electron microscope (TEM) images of Ag, AgT, Au, and AuT NPs. **b**, an illustration of multiple-core-shell TAuT structure, and TEM images of TiO_2 core as a template, TiO_2 core with Au seeds coating, TiO_2 with continuous Au shell, and TAuT NP annealed at 500°C. All scale bars are 5 nm.

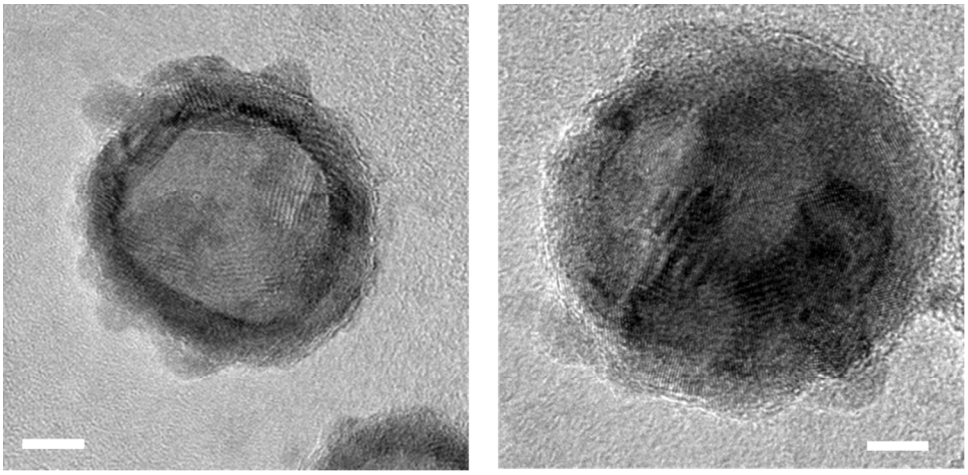

Figure S5. TEM images of TAuT NPs focused on the gold shell layer (left) and focused on the TiO_2 shell layer (right). These TEM images clearly show the multiple-core-shell oxide-metal-oxide structure of the TAuT NPs. All scale bars are 5 nm.

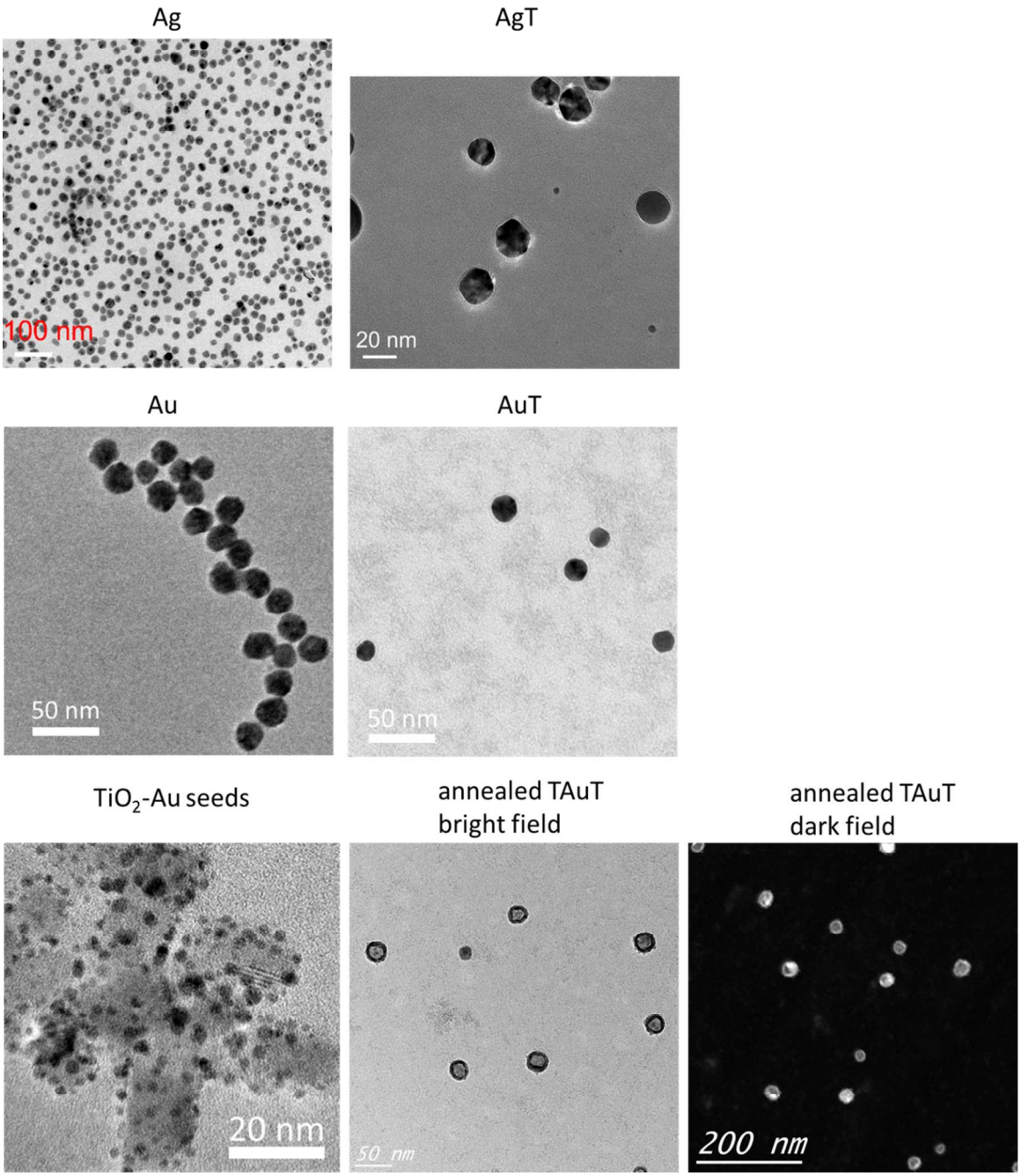

Figure S6. Low magnification TEM images of Ag, AgT, Au, AuT, TiO_2-Au seeds, and TAuT (bright field and dark field) NPs. The uniform synthesis for all NPs used in this report is illustrated.

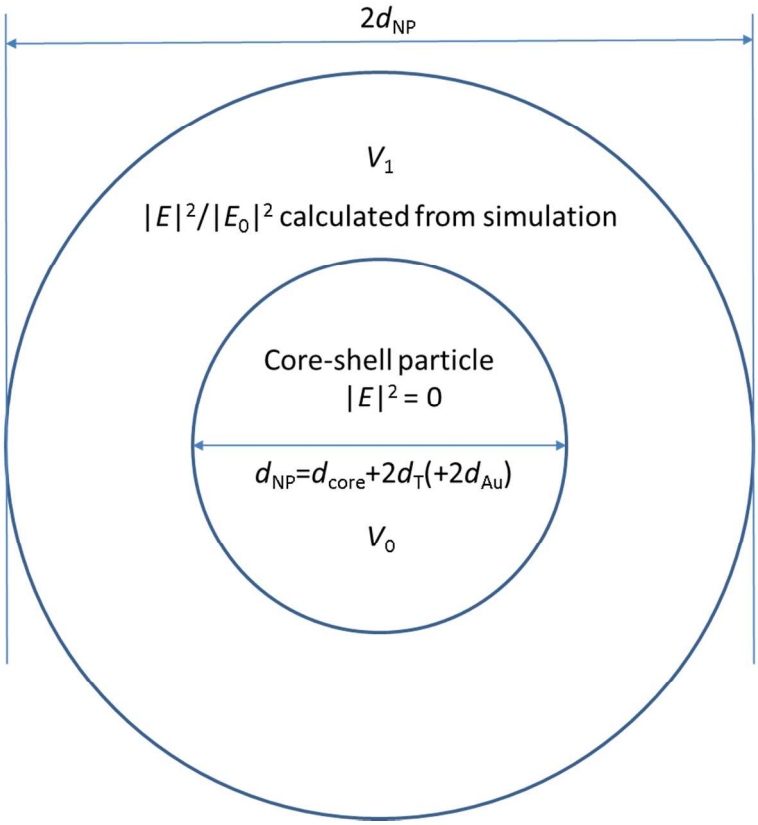

Figure S7. Schematic illustration for deriving the enhancement factor.

$$\text{Enhancement Factor}(\lambda) = \frac{|E|^2_{\text{int}}}{|E_0|^2_{\text{int}}}(\lambda) = \int_0^{2\pi}\int_0^{\pi}\int_0^{2R_{\text{CS}}} \frac{|E(r,\theta,\phi,\lambda)|^2}{|E_0(r,\theta,\phi,\lambda)|^2} r^2 \sin\theta \, \mathrm{d}r\mathrm{d}\theta\mathrm{d}\phi,$$

$|E(r,\theta,\phi,\lambda)|^2 = 0$ when $0 \le r \le R_{\text{CS}}$.

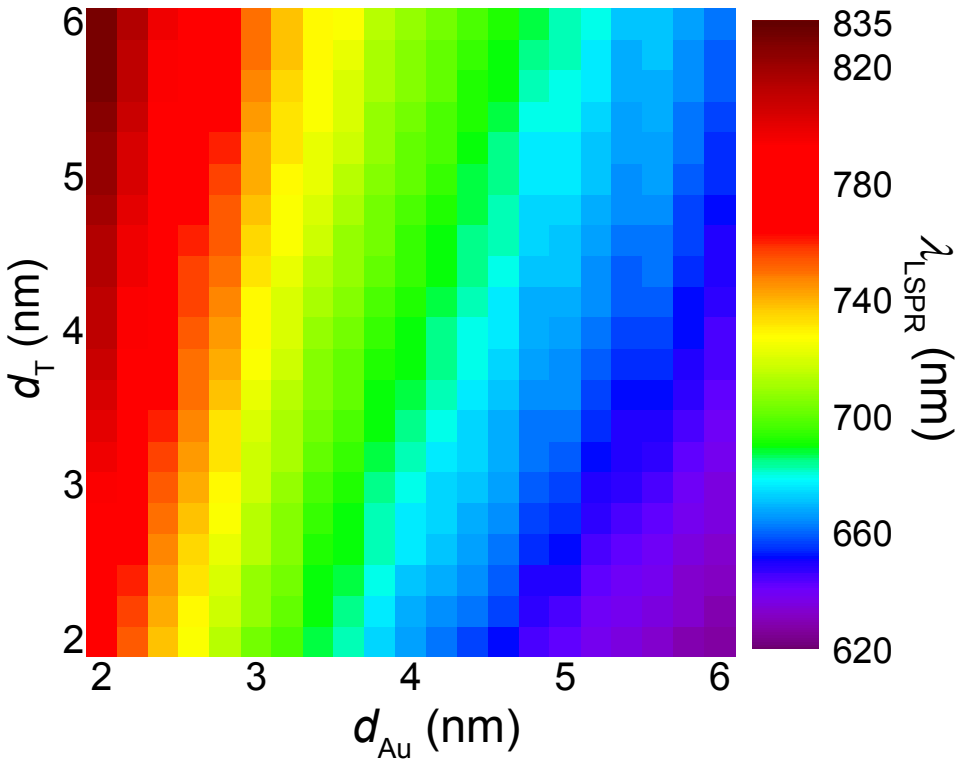

Figure S8. λ_{LSPR} of TAuT NPs as a function of d_{Au} and d_T.

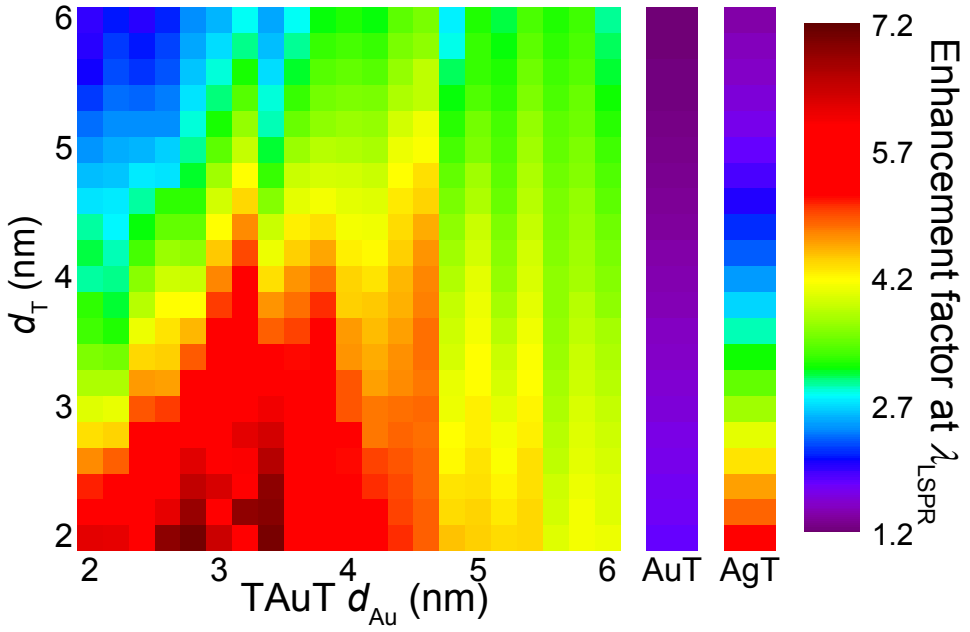

Figure S9. Enhancement factor at λ_{LSPR} as a function of d_{Au} (of TAuT) and d_T (of AgT, AuT, and TAuT).

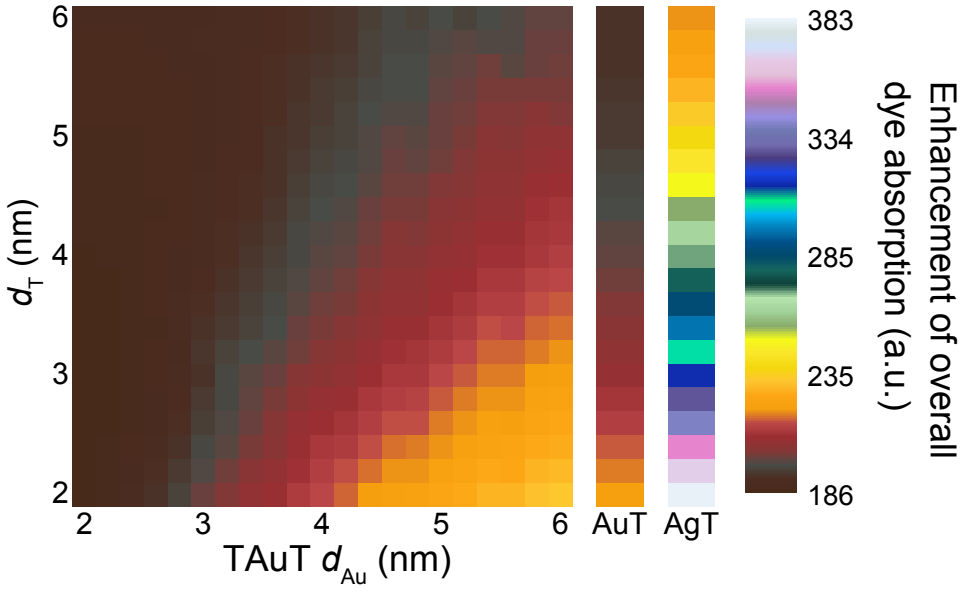

Figure S10. Enhancement of overall dye absorption as a function of d_{Au} (of TAuT) and d_T (of AgT, AuT, and TAuT).

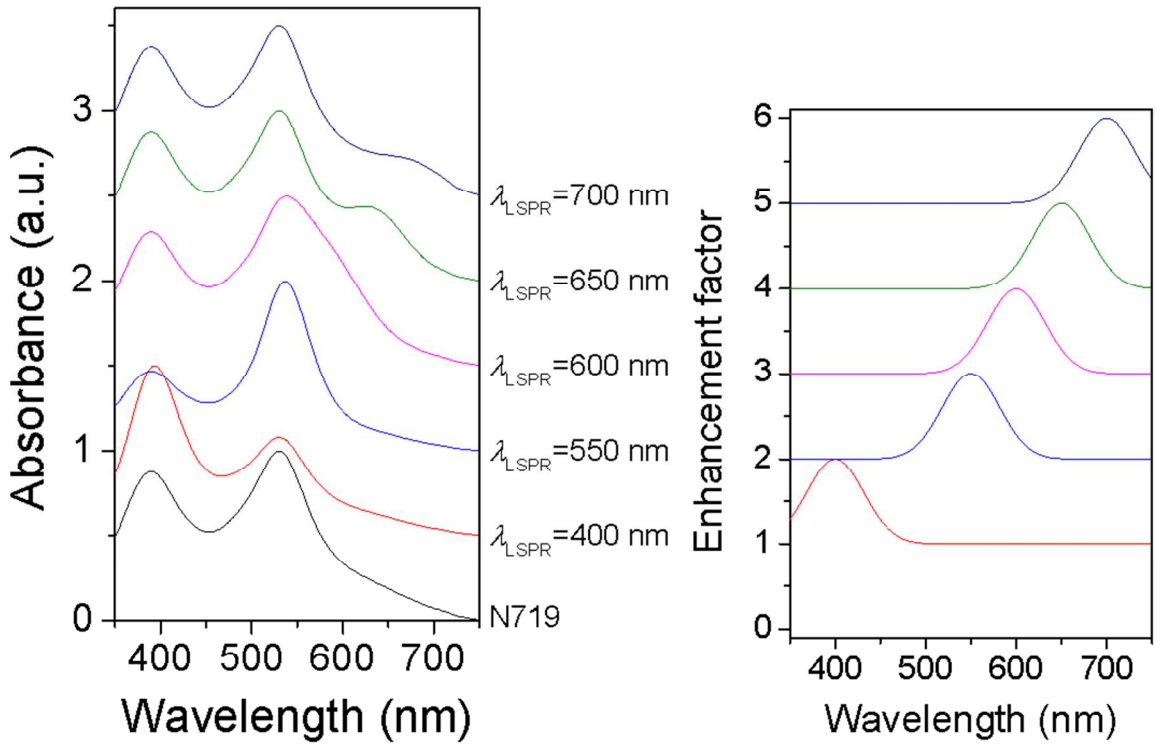

Figure S11. Simulated absorption spectra of N719 by matching λ_{LSPR} and λ_{Hi} or λ_{Lo}. On the left, simulated absorption spectra of N719 enhanced by plasmonic NPs with λ_{LSPR} from 400 to 700 nm. Each spectrum is normalized by the maximum absorbance in the visible region. On the right, the enhancement factors as a function of wavelength are represented by Gaussian distributions (each curve in the graph has a Y-offset value of 1). When the λ_{LSPR} is between 400 to 550 nm, the optical absorption at strong-absorption range of dye-molecules is enhanced, and the spectral shape is more unbalanced compared to the original optical absorption of N719. When the λ_{LSPR} is between 600 to 700 nm, the optical absorption at weak-absorption range of dye-molecules is enhanced, and the spectral shape is more balanced compared to the original optical absorption of N719.

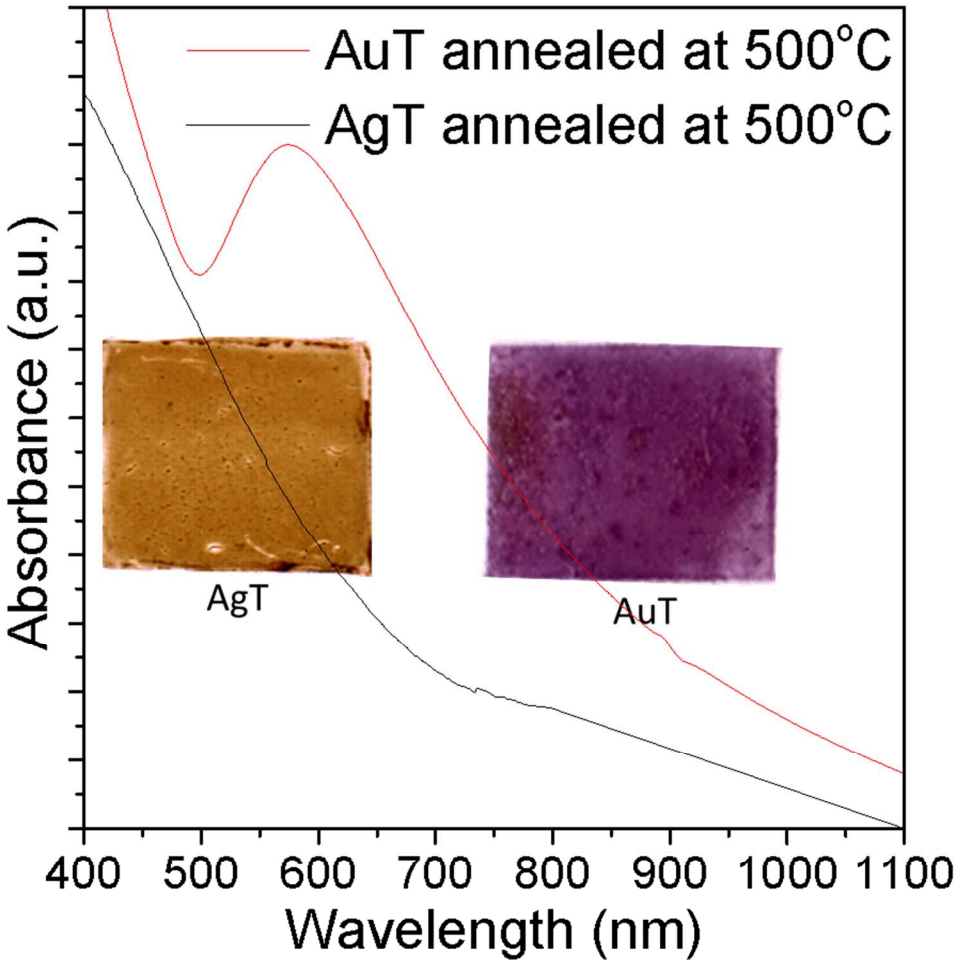

Figure S12. Thermal stability of AgT and AuT NPs. Photograph images and absorption spectra of thin films of AgT (left) and AuT (right) on glass substrates after 500°C annealing; both AgT and AuT NPs maintain their structural and optical properties, as expected.

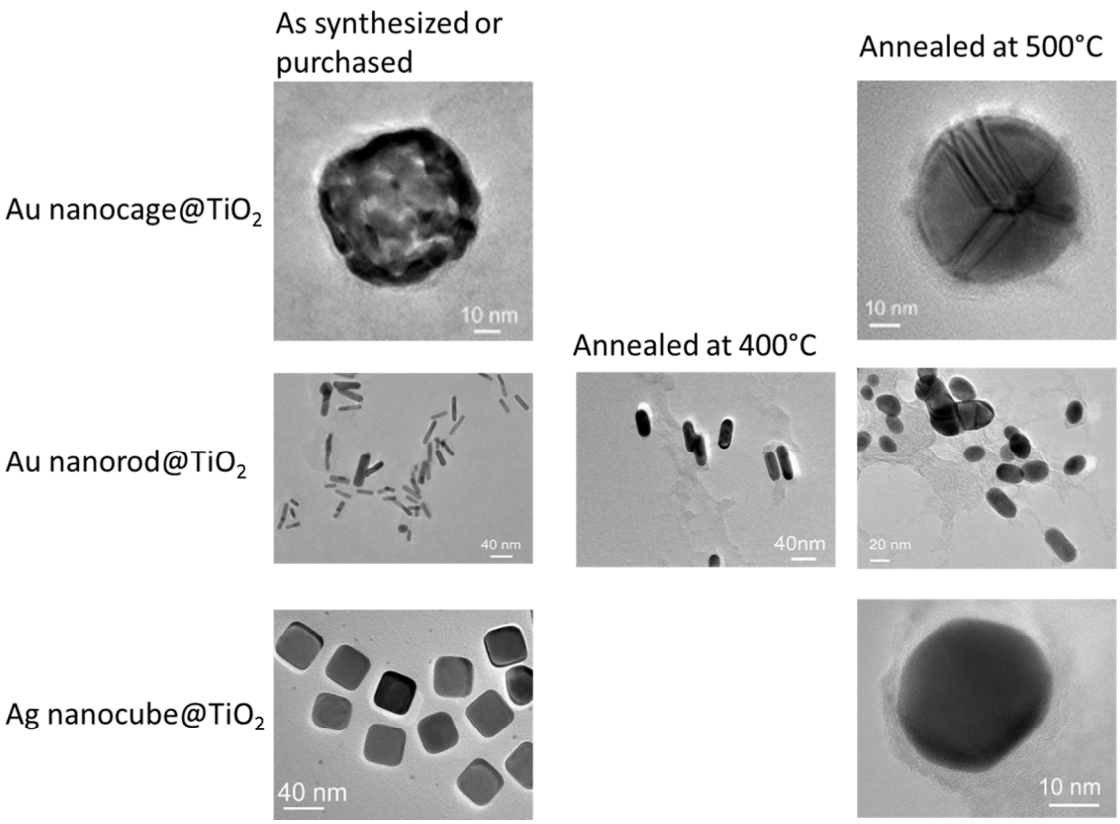

Figure S13. Thermal stability of other geometries of plasmonic NPs. TEM images of gold nanocage@TiO_2, gold nanorod@TiO_2, and silver nanocube@TiO_2 before and after 500°C annealing; after annealing, the gold nanocages and silver nanocubes melt and form spherical structures, and the gold nanorods melt to form spheroidal or spherical structures.

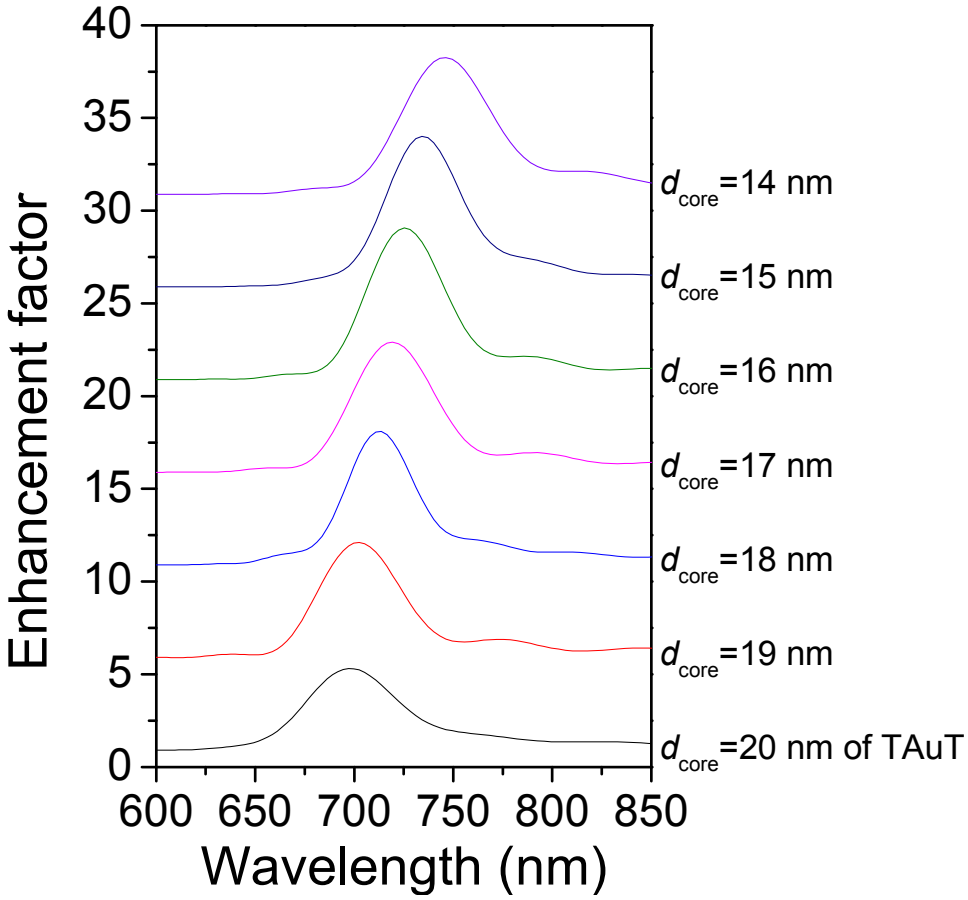

Figure S14. TAuT core effect. Enhancement factor as a function of wavelength for TAuT NPs with different d_{core} (d_{Au}=2 nm, d_T=2 nm). Each curve in the graph has a Y-offset value of 5. Comparing to changing d_{Au} and d_T, changing d_{core} has a smaller effect on the λ_{LSPR} and enhancement factor.

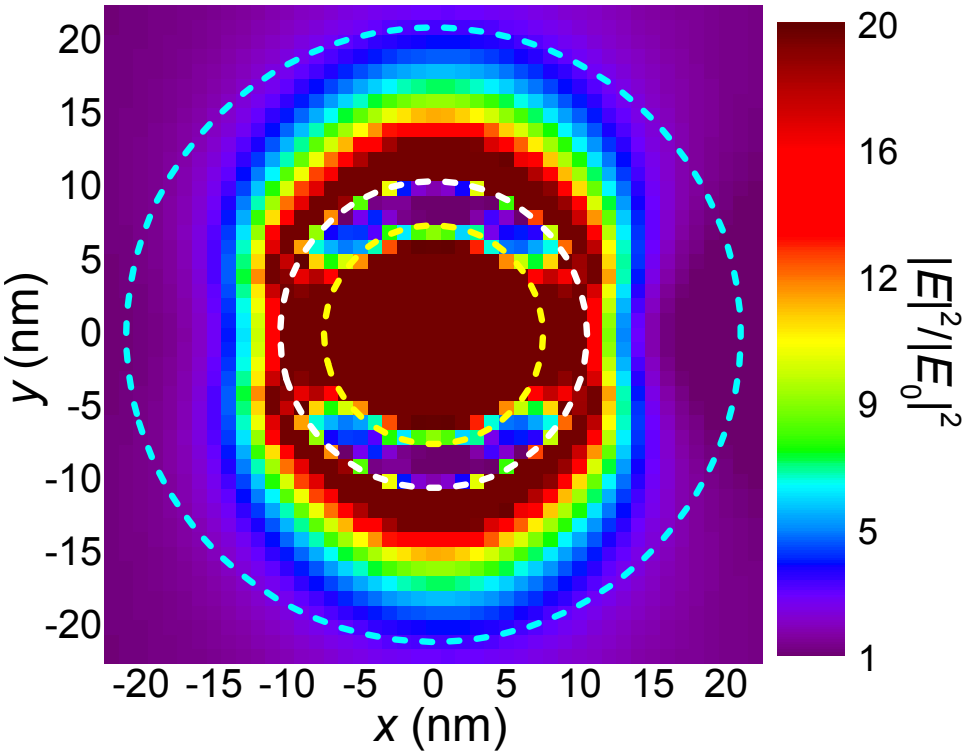

Figure S15. Simulated EM intensity enhancement ($|E|^2/|E_0|^2$) in near field at λ_{LSPR} for a hollow gold nanoshell (d_{inner_sphere}=15 nm, d_{Au}=3 nm). The inner circles (white and yellow) represent the inner and outer spheres of the hollow gold nanoshell, and the outermost circles (cyan) represent the volume of integration.

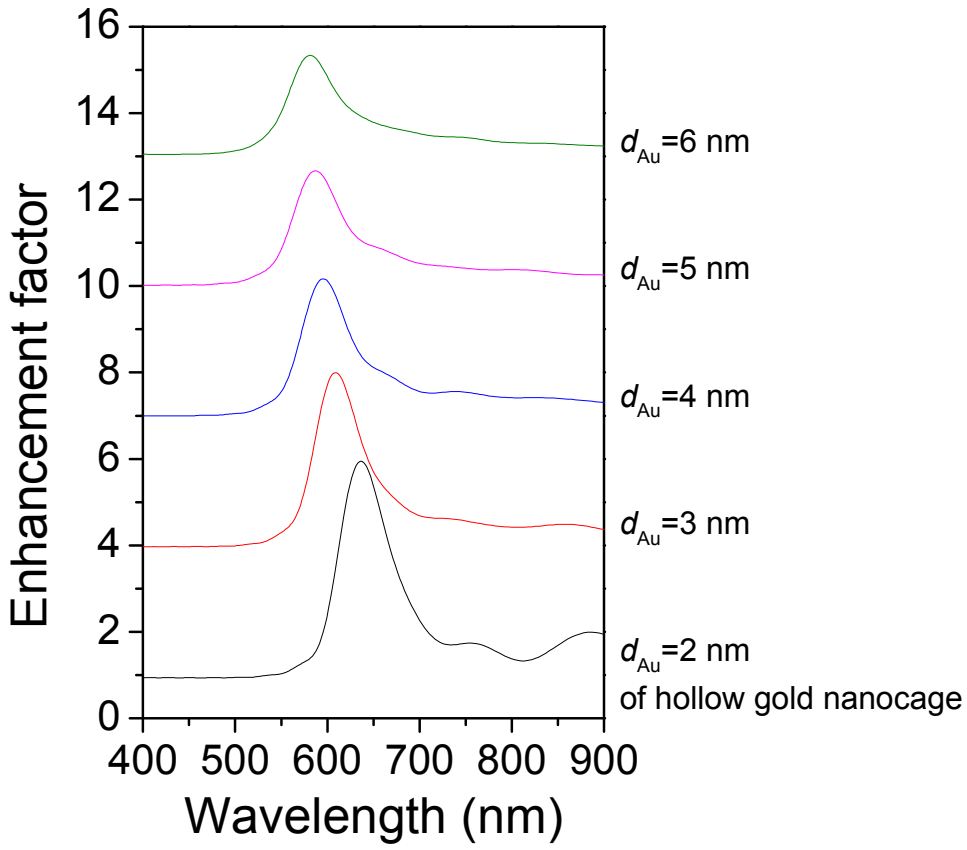

Figure S16. Enhancement factor as a function of wavelength for hollow gold nanoshells with different d_{Au} (d_{inner_sphere}=15 nm). Each curve in the graph has a Y-offset value of 3.

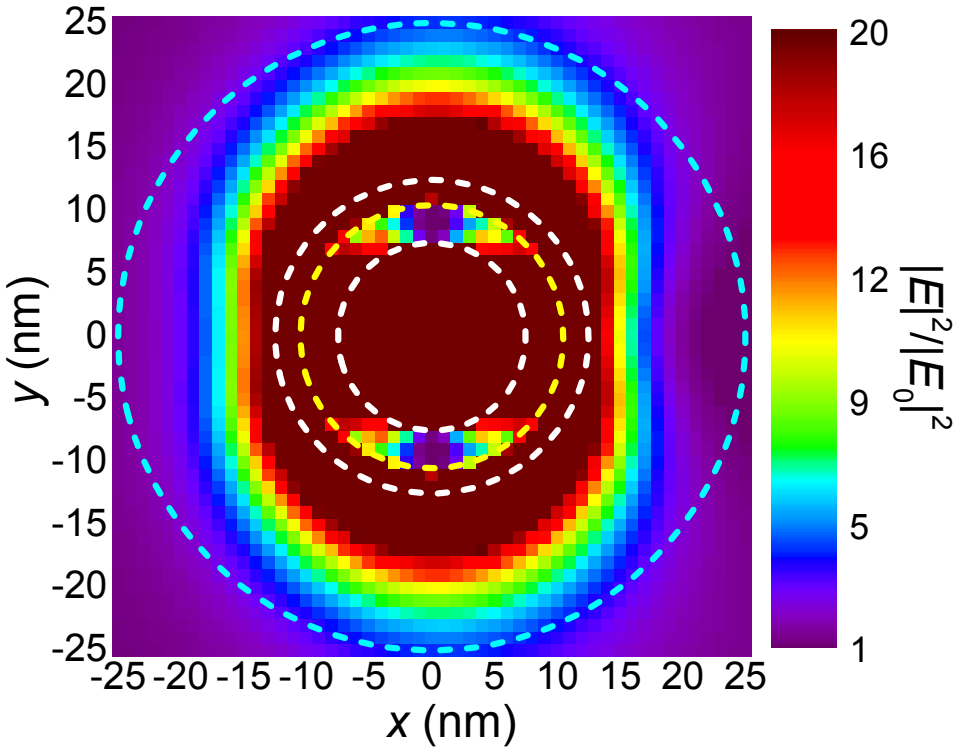

Figure S17. Simulated EM intensity enhancement ($|E|^2/|E_0|^2$) in near field at λ_{LSPR} for TAgT NPs (d_{core}=15 nm, d_{Ag}=3 nm, d_T=2 nm). The inner circles (white and yellow) represent different layers of NPs, and the outer most circles (cyan) represent the volume of integration.

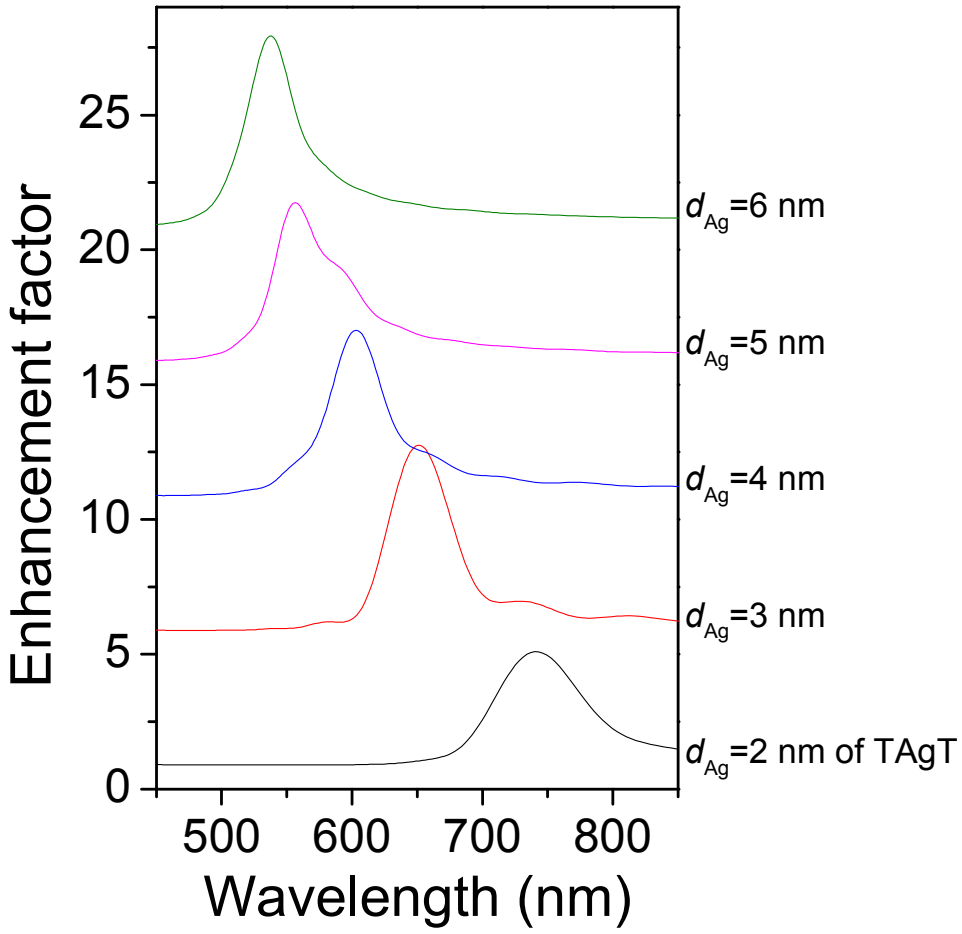

Figure S18. Enhancement factor as a function of wavelength for TAgT NPs with different d_{Ag} (d_{core}=15 nm, d_T=2 nm). Each curve in the graph has a Y-offset value of 5.

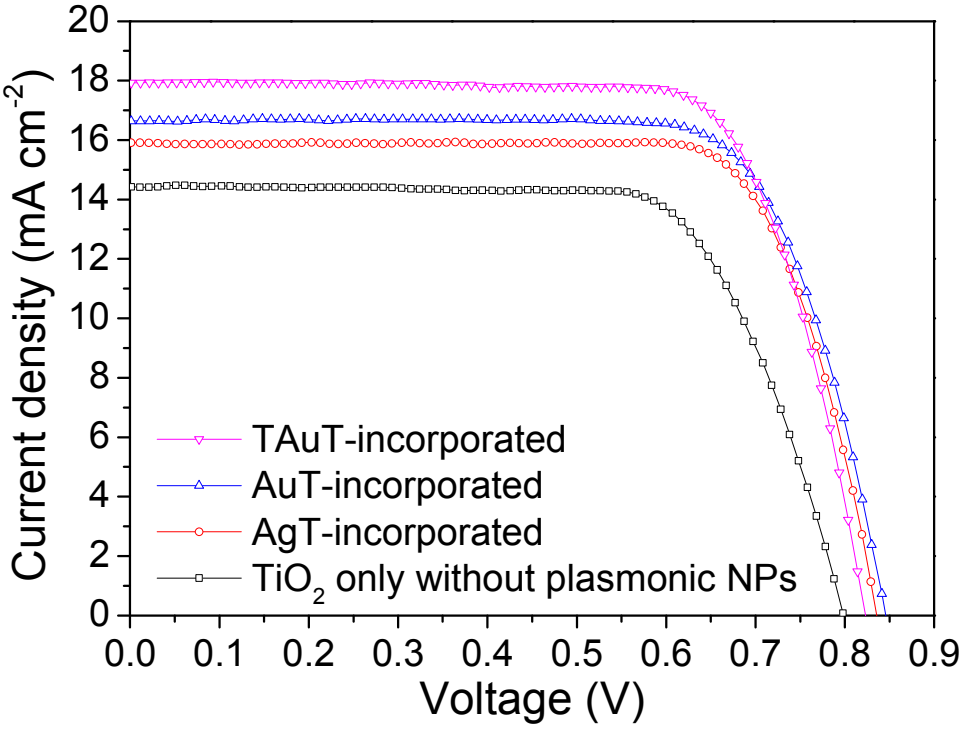

Figure S19. J-V curves of optically-thick photoanodes of TiO_2 without plasmonic NPs, AgT (1.0 wt%), AuT (1.8 wt%), and TAuT (3.2 wt%) NPs blended with TiO_2 NPs for optimized PCE under AM 1.5 illumination.

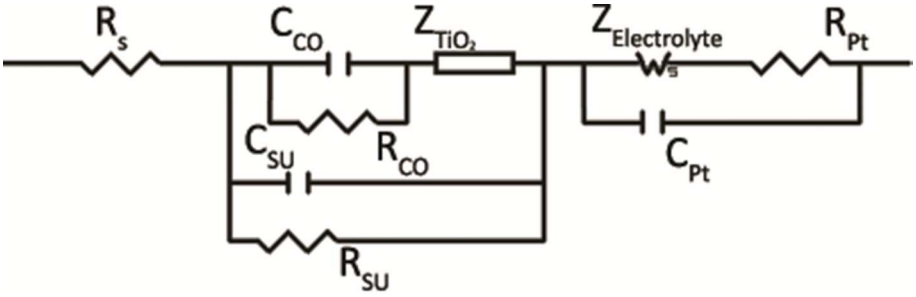

Figure S20. Equivalent circuit impedance model of DSSCs. R_s: ohmic series resistance of the cell. R_{CO} and C_{CO}: contact resistance and capacitance at the interface between the conducting substrate and the TiO_2 photoanode film. R_{SU} and C_{SU}: charge transfer resistance and double layer capacitance at the substrate/electrolyte interface. R_{Pt} and C_{Pt}: charge transfer resistance and double layer capacitance at the counter electrode-electrolyte interface. Z_{TiO2}: transmission line impedance of the TiO_2 photoanode film consisting of the elements R_T (resistivity of electron transport in the photoanode film), R_{REC} (charge recombination resistance at the TiO_2/dye/electrolyte interface), and C_μ (chemical capacitance of the photoanode film). $Z_{electrolyte}$: mass transport impedance at the counter electrode.

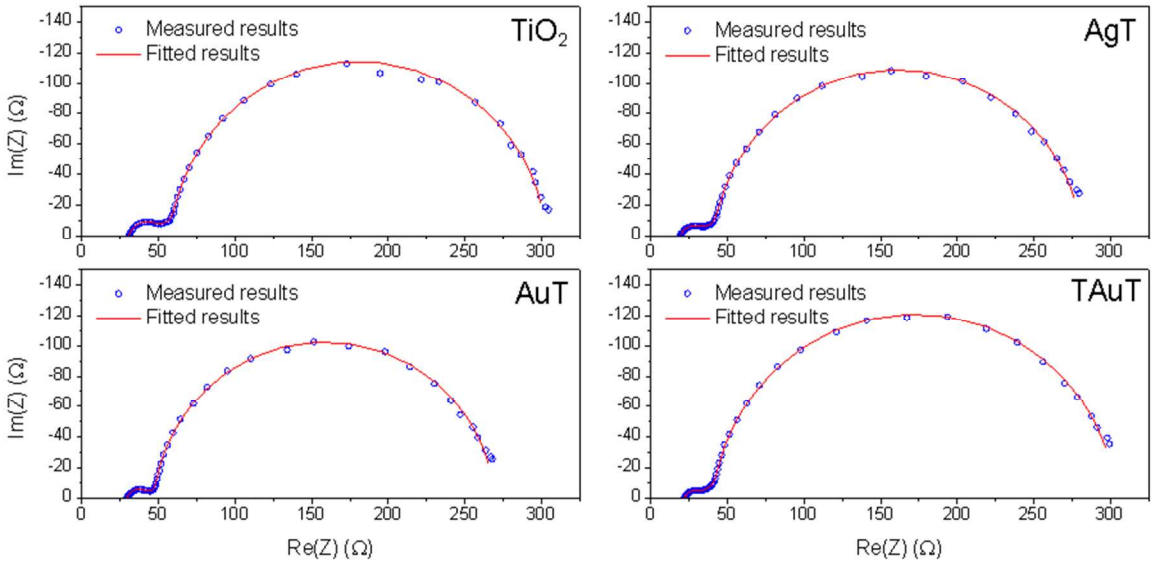

Figure S21. Nyquist diagrams of the electrochemical impedance spectra obtained under dark condition for different devices. Experimental data are presented by symbols, and fitted results using the equivalent circuit in Figure S20 are shown as solid lines. The bias applied to all the devices during measurement is 600 mV. EIS spectra of four DSSCs: with only TiO_2 NPs, with AgT (1.0 wt%), AuT (1.8 wt%), and TAuT (3.2 wt%) NPs-incorporated photoanodes are measured. The highest concentration for each plasmonic NPs investigated in this report has been utilized for the electrochemical impedance spectra measurement.

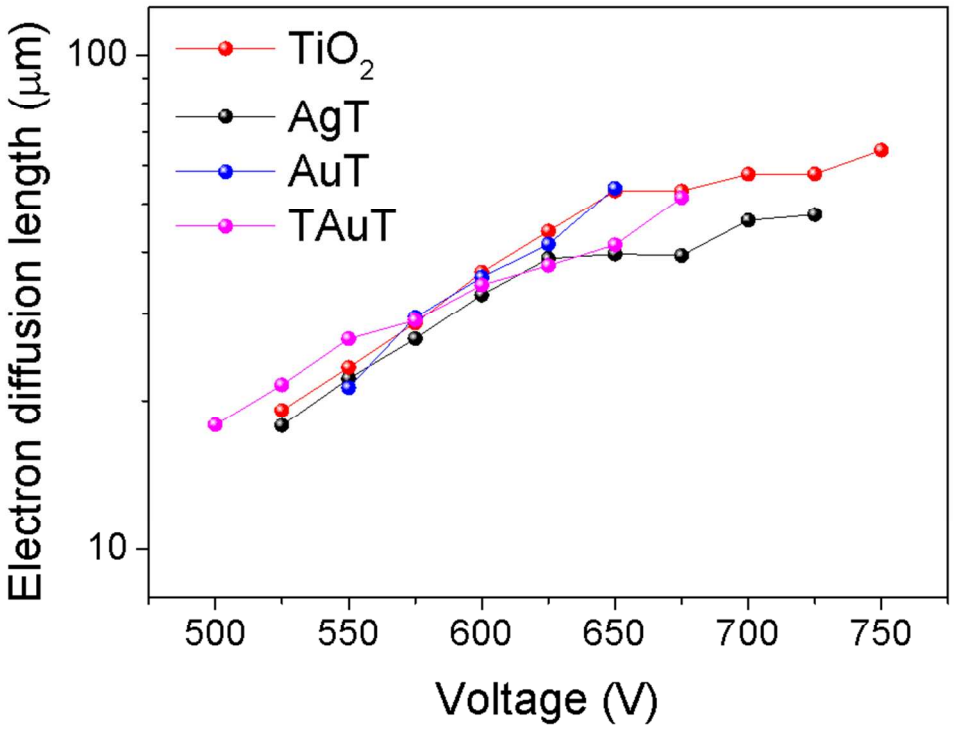

Figure S22. Electron diffusion lengths of four DSSCs: with only TiO_2 NPs, with AgT (1.0 wt%), AuT (1.8 wt%), and TAuT (3.2 wt%) NPs-incorporated photoanodes. The highest concentration for each plasmonic NPs investigated in this report has been utilized for the electron diffusion length measurement.

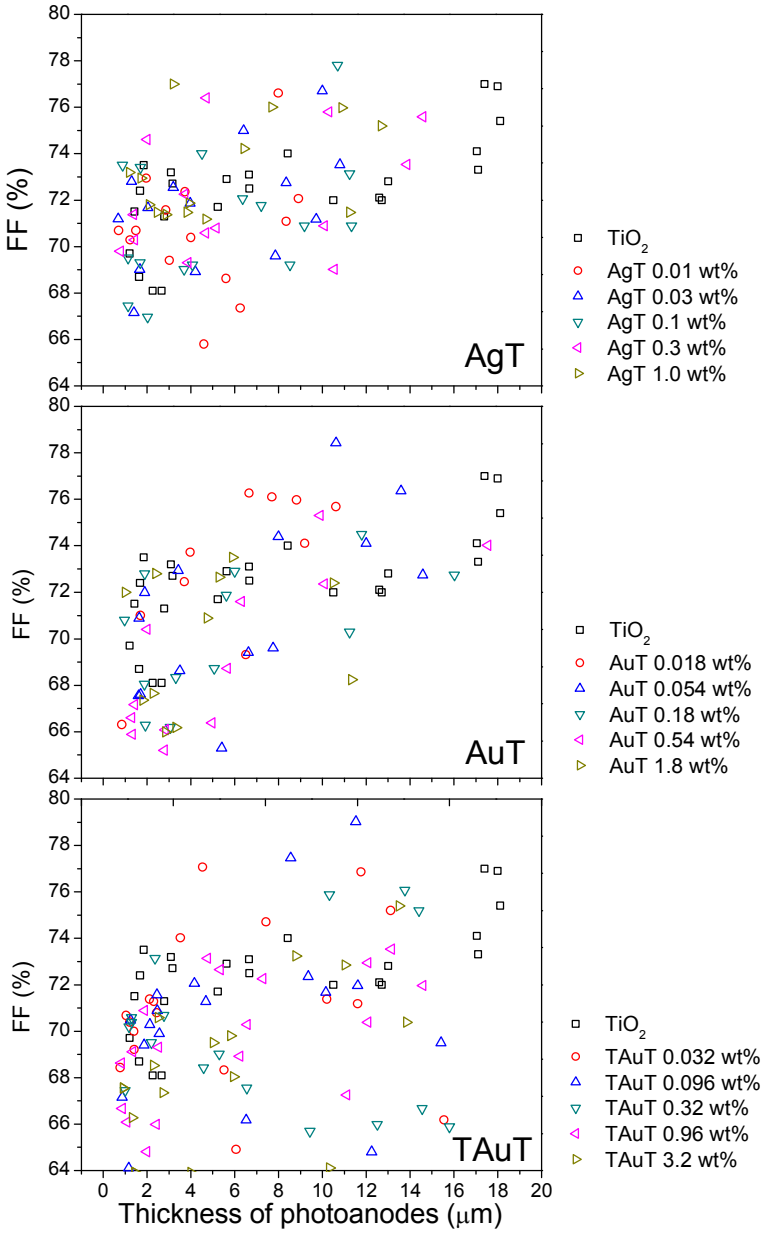

Figure S23. Fill factors of tunable LSP-enhanced DSSCs with AgT, AuT, and TAuT NPs-incorporated photoanodes, as a function of the concentration of plasmonic NPs (0-3.2 wt%) and thickness of photoanodes (1-20 μm).

Table S1. Device performance of DSSCs shown in figure 3b,c,d, including incorporated plasmonic NPs, the concentration of plasmonic NPs, thicknesses, V_{OC}, $J_{SC,}$ FF, and PCE.

Plasmonic NPs	Concentration /wt%	Thickness /μm	V_{OC} /mV	J_{SC} /mA cm^{-2}	FF /%	PCE /%
TiO_2		1.21	899	4.55	69.7	2.85
TiO_2		1.44	863	5.41	71.5	3.34
TiO_2		1.64	881	5.67	68.7	3.43
TiO_2		1.69	863	5.62	72.4	3.51
TiO_2		1.85	875	5.98	73.5	3.85
TiO_2		2.26	881	7.06	68.1	4.23
TiO_2		2.67	845	7.90	68.1	4.55
TiO_2		2.78	893	6.99	71.3	4.45
TiO_2		3.09	874	7.52	73.2	4.81
TiO_2		3.17	859	8.46	72.7	5.28
TiO_2		5.23	841	10.09	71.7	6.08
TiO_2		5.63	834	10.65	72.9	6.48
TiO_2		6.66	838	11.23	73.1	6.88
TiO_2		6.67	823	10.99	72.5	6.56
TiO_2		8.42	821	11.18	74.0	6.79
TiO_2		10.50	810	13.48	72.0	7.86
TiO_2		12.60	805	13.17	72.1	7.65
TiO_2		12.72	821	13.98	72.0	8.26
TiO_2		13.01	799	14.31	72.8	8.32
TiO_2		17.04	782	13.23	74.1	7.67
TiO_2		17.10	778	13.20	73.3	7.53
TiO_2		17.40	796	12.41	77.0	7.61
TiO_2		18.00	781	12.41	76.9	7.46
TiO_2		18.11	794	13.14	75.4	7.86
AgT	0.01	0.70	890	3.00	70.7	1.89
AgT	0.01	1.22	911	6.21	70.3	3.98
AgT	0.01	1.50	891	7.37	70.7	4.64
AgT	0.01	1.97	878	7.61	72.9	4.87
AgT	0.01	2.86	873	9.64	71.6	6.02
AgT	0.01	3.02	888	9.89	69.4	6.10
AgT	0.01	3.74	873	10.78	72.4	6.81
AgT	0.01	4.01	872	11.41	70.4	7.00
AgT	0.01	4.60	859	13.12	65.8	7.42
AgT	0.01	5.61	879	11.84	68.6	7.14
AgT	0.01	6.26	864	12.47	67.4	7.26
AgT	0.01	8.00	835	14.37	76.6	9.19
AgT	0.01	8.35	855	12.68	71.1	7.71
AgT	0.01	8.91	852	12.79	72.1	7.85

Plasmonic NPs	Concentration /wt%	Thickness /μm	V_{OC} /mV	J_{SC} /mA cm^{-2}	FF /%	PCE /%
AgT	0.03	0.69	893	3.00	71.2	1.91
AgT	0.03	1.30	893	5.12	72.8	3.33
AgT	0.03	1.40	900	6.72	67.2	4.06
AgT	0.03	1.67	885	7.23	69.0	4.42
AgT	0.03	2.04	885	8.75	71.7	5.55
AgT	0.03	3.20	886	10.02	72.5	6.44
AgT	0.03	3.97	874	11.54	71.9	7.24
AgT	0.03	4.20	870	12.55	68.9	7.53
AgT	0.03	6.40	851	12.49	75.0	7.97
AgT	0.03	7.86	854	12.68	69.6	7.54
AgT	0.03	8.35	857	12.68	72.7	7.91
AgT	0.03	9.72	832	13.74	71.2	8.14
AgT	0.03	10.00	824	13.43	76.7	8.49
AgT	0.03	10.80	831	13.74	73.5	8.39
AgT	0.1	0.88	906	4.00	73.5	2.66
AgT	0.1	1.13	873	4.95	67.5	2.91
AgT	0.1	1.14	877	4.69	69.5	2.86
AgT	0.1	1.69	867	7.61	69.3	4.57
AgT	0.1	1.70	889	6.25	73.4	4.08
AgT	0.1	2.03	879	9.26	67.0	5.45
AgT	0.1	3.69	863	11.29	69.0	6.72
AgT	0.1	4.08	863	12.30	69.2	7.35
AgT	0.1	4.50	860	12.39	74.0	7.89
AgT	0.1	6.35	850	12.58	72.1	7.70
AgT	0.1	7.20	833	13.21	71.8	7.90
AgT	0.1	8.52	841	14.27	69.2	8.31
AgT	0.1	9.18	816	15.22	70.9	8.81
AgT	0.1	10.70	830	14.79	77.8	9.55
AgT	0.1	11.25	838	15.85	73.1	9.72
AgT	0.1	11.34	828	13.53	70.9	7.94
AgT	0.3	0.78	888	3.25	69.8	2.01
AgT	0.3	1.40	891	8.24	71.4	5.24
AgT	0.3	1.43	910	7.61	70.3	4.87
AgT	0.3	2.00	896	7.12	74.6	4.76
AgT	0.3	3.73	878	12.30	72.3	7.80
AgT	0.3	3.86	877	12.94	69.3	7.86
AgT	0.3	4.67	875	12.68	70.6	7.83
AgT	0.3	4.70	869	10.83	76.4	7.19
AgT	0.3	5.14	868	11.73	70.8	7.21
AgT	0.3	10.08	837	14.06	70.9	8.34
AgT	0.3	10.30	836	15.93	75.8	10.10
AgT	0.3	10.53	839	14.80	69.0	8.57
AgT	0.3	13.86	818	13.00	73.5	7.82

Plasmonic NPs	Concentration /wt%	Thickness /μm	V_{OC} /mV	J_{SC} /mA cm^{-2}	FF /%	PCE /%
AgT	0.3	14.58	822	12.68	75.6	7.88
AgT	1.0	1.20	906	3.87	73.2	2.57
AgT	1.0	1.73	864	6.85	72.9	4.32
AgT	1.0	2.10	887	8.62	71.8	5.49
AgT	1.0	2.48	886	9.38	71.5	5.94
AgT	1.0	2.88	883	10.15	71.4	6.39
AgT	1.0	3.20	895	10.00	77.0	6.89
AgT	1.0	3.82	856	11.16	71.5	6.83
AgT	1.0	3.93	873	11.20	71.9	7.02
AgT	1.0	4.68	863	13.06	71.2	8.03
AgT	1.0	6.43	836	14.37	74.2	8.92
AgT	1.0	7.70	857	13.02	76.0	8.48
AgT	1.0	10.89	838	15.85	76.0	10.10
AgT	1.0	11.25	838	15.43	71.5	9.24
AgT	1.0	12.69	828	14.37	75.2	8.95
AuT	0.018	0.85	908	2.99	66.3	1.80
AuT	0.018	1.70	883	5.09	71.0	3.19
AuT	0.018	1.75	904	9.09	63.0	5.18
AuT	0.018	3.70	892	11.49	72.5	7.43
AuT	0.018	3.98	899	12.45	73.7	8.24
AuT	0.018	6.51	846	13.40	69.3	7.85
AuT	0.018	6.66	852	11.37	76.3	7.39
AuT	0.018	7.70	820	11.96	76.1	7.46
AuT	0.018	8.82	843	13.28	76.0	8.51
AuT	0.018	9.20	794	15.06	74.1	8.86
AuT	0.018	10.62	833	13.88	75.7	8.75
AuT	0.054	1.61	910	9.57	67.5	5.88
AuT	0.054	1.65	909	7.90	70.9	5.09
AuT	0.054	1.70	892	6.98	67.6	4.21
AuT	0.054	1.90	895	6.09	72.0	3.93
AuT	0.054	3.42	853	9.21	72.9	5.73
AuT	0.054	3.50	885	11.97	68.6	7.27
AuT	0.054	5.41	848	12.45	65.3	6.89
AuT	0.054	6.63	841	14.72	69.4	8.60
AuT	0.054	7.76	830	15.92	69.6	9.19
AuT	0.054	8.00	825	10.08	74.4	6.19
AuT	0.054	10.62	826	14.24	78.4	9.22
AuT	0.054	12.00	810	15.84	74.1	9.51
AuT	0.054	13.59	812	15.68	76.4	9.72
AuT	0.054	14.58	811	15.92	72.7	9.39
AuT	0.18	0.98	900	4.54	70.8	2.89
AuT	0.18	1.87	906	7.78	68.0	4.79
AuT	0.18	1.90	865	7.42	72.8	4.67

Plasmonic NPs	Concentration /wt%	Thickness /μm	V_{OC} /mV	J_{SC} /mA cm^{-2}	FF /%	PCE /%
AuT	0.18	1.93	898	9.69	66.3	5.77
AuT	0.18	3.06	884	11.01	66.2	6.44
AuT	0.18	3.32	893	11.13	68.3	6.79
AuT	0.18	5.08	863	12.45	68.7	7.38
AuT	0.18	5.62	869	13.04	71.9	8.15
AuT	0.18	6.00	830	13.84	72.9	8.38
AuT	0.18	11.25	824	16.63	70.3	9.63
AuT	0.18	11.80	803	14.84	74.5	8.88
AuT	0.18	16.02	813	14.72	72.7	8.71
AuT	0.54	1.30	889	6.20	66.6	3.67
AuT	0.54	1.32	908	8.50	65.9	5.08
AuT	0.54	1.43	901	6.70	67.2	4.05
AuT	0.54	2.00	886	6.20	70.4	3.87
AuT	0.54	2.78	899	10.89	65.2	6.38
AuT	0.54	2.84	883	11.13	66.1	6.49
AuT	0.54	4.97	863	13.76	66.4	7.88
AuT	0.54	5.66	868	13.64	68.7	8.14
AuT	0.54	6.30	806	14.51	71.6	8.37
AuT	0.54	9.90	806	15.51	75.3	9.41
AuT	0.54	10.08	846	16.75	72.4	10.25
AuT	0.54	17.55	823	15.92	74.0	9.69
AuT	1.8	1.00	881	4.65	72.0	2.95
AuT	1.8	1.80	900	8.02	67.4	4.86
AuT	1.8	2.29	893	9.93	67.6	6.00
AuT	1.8	2.40	869	7.75	72.8	4.90
AuT	1.8	2.84	880	10.41	66.0	6.04
AuT	1.8	3.31	904	12.45	66.2	7.44
AuT	1.8	4.74	879	12.56	70.9	7.83
AuT	1.8	5.29	877	13.52	72.6	8.61
AuT	1.8	5.90	842	13.51	73.5	8.36
AuT	1.8	10.50	802	17.61	72.4	10.23
AuT	1.8	11.34	841	17.11	68.2	9.82
TAuT	0.032	0.78	881	3.91	68.4	2.36
TAuT	0.032	1.05	904	5.13	70.7	3.28
TAuT	0.032	1.22	881	5.36	70.4	3.32
TAuT	0.032	1.41	876	6.49	70.0	3.98
TAuT	0.032	1.42	913	6.50	69.2	4.11
TAuT	0.032	2.12	878	8.03	71.4	5.04
TAuT	0.032	2.30	897	9.01	71.3	5.76
TAuT	0.032	2.45	882	9.35	70.8	5.84
TAuT	0.032	3.53	861	9.37	74.0	5.97
TAuT	0.032	4.54	838	8.14	77.1	5.26
TAuT	0.032	5.52	853	13.91	68.3	8.10

Plasmonic NPs	Concentration /wt%	Thickness /μm	V_{OC} /mV	J_{SC} /mA cm^{-2}	FF /%	PCE /%
TAuT	0.032	6.07	835	14.25	64.9	7.73
TAuT	0.032	7.43	825	13.39	74.7	8.25
TAuT	0.032	10.21	829	16.76	71.4	9.92
TAuT	0.032	11.62	817	14.48	71.2	8.42
TAuT	0.032	11.76	811	12.26	76.9	7.64
TAuT	0.032	13.12	808	13.60	75.2	8.26
TAuT	0.032	14.40	795	12.88	85.5	8.75
TAuT	0.032	15.55	799	18.92	66.2	10.00
TAuT	0.096	0.87	858	4.33	67.2	2.49
TAuT	0.096	1.17	862	5.15	64.1	2.85
TAuT	0.096	1.25	925	5.70	70.5	3.72
TAuT	0.096	1.86	899	8.44	69.4	5.26
TAuT	0.096	2.14	869	8.34	70.3	5.10
TAuT	0.096	2.46	863	9.17	71.6	5.66
TAuT	0.096	2.48	893	10.37	70.9	6.56
TAuT	0.096	2.57	878	10.15	69.9	6.23
TAuT	0.096	4.17	851	10.61	72.1	6.50
TAuT	0.096	4.68	851	10.40	71.3	6.31
TAuT	0.096	6.42	825	17.67	49.6	7.23
TAuT	0.096	6.53	833	13.91	66.2	7.67
TAuT	0.096	8.56	814	11.43	77.5	7.21
TAuT	0.096	9.36	815	11.85	72.4	6.98
TAuT	0.096	10.16	808	12.57	71.7	7.28
TAuT	0.096	11.52	804	13.39	79.0	8.50
TAuT	0.096	11.61	804	17.10	72.0	9.89
TAuT	0.096	12.26	806	15.85	64.8	8.27
TAuT	0.096	15.07	781	16.99	62.2	8.25
TAuT	0.096	15.41	786	16.30	69.5	8.91
TAuT	0.32	1.01	849	4.84	67.5	2.77
TAuT	0.32	1.18	913	6.16	70.2	3.94
TAuT	0.32	1.30	870	5.15	70.6	3.16
TAuT	0.32	1.31	912	6.50	70.4	4.17
TAuT	0.32	2.21	882	9.58	69.5	5.87
TAuT	0.32	2.31	857	9.35	52.8	4.23
TAuT	0.32	2.38	873	9.06	73.1	5.79
TAuT	0.32	2.77	856	8.55	70.7	5.17
TAuT	0.32	4.58	853	11.02	68.4	6.43
TAuT	0.32	5.29	845	11.74	69.0	6.84
TAuT	0.32	5.36	821	14.36	62.2	7.33
TAuT	0.32	6.56	817	14.48	67.5	7.99
TAuT	0.32	9.44	815	12.57	65.7	6.73
TAuT	0.32	10.32	819	13.29	75.9	8.26
TAuT	0.32	11.75	794	15.85	63.5	7.99

Plasmonic NPs	Concentration /wt%	Thickness /μm	V_{OC} /mV	J_{SC} /mA cm^{-2}	FF /%	PCE /%
TAuT	0.32	12.50	783	18.24	66.0	9.43
TAuT	0.32	13.76	808	14.83	76.1	9.12
TAuT	0.32	14.40	818	15.73	75.2	9.68
TAuT	0.32	14.56	803	15.35	66.7	8.21
TAuT	0.32	15.80	784	18.35	65.9	9.48
TAuT	0.96	0.83	921	4.90	68.6	3.10
TAuT	0.96	0.87	921	4.56	66.7	2.80
TAuT	0.96	1.08	863	4.74	66.1	2.70
TAuT	0.96	1.34	856	6.18	69.1	3.66
TAuT	0.96	1.88	886	9.12	70.9	5.73
TAuT	0.96	1.98	854	8.55	64.8	4.73
TAuT	0.96	2.41	897	10.72	66.0	6.34
TAuT	0.96	2.51	855	9.37	69.3	5.55
TAuT	0.96	4.76	860	10.82	73.1	6.80
TAuT	0.96	5.34	850	11.64	72.6	7.18
TAuT	0.96	6.23	846	14.93	68.9	8.70
TAuT	0.96	6.57	849	15.85	70.3	9.45
TAuT	0.96	7.12	803	13.29	60.7	6.47
TAuT	0.96	7.28	835	13.49	72.3	8.14
TAuT	0.96	11.12	816	18.13	67.3	9.95
TAuT	0.96	12.08	804	15.14	72.9	8.88
TAuT	0.96	12.08	807	14.73	70.4	8.37
TAuT	0.96	13.15	806	18.13	73.5	10.74
TAuT	0.96	14.59	812	18.13	72.0	10.59
TAuT	3.2	0.92	915	5.24	67.5	3.24
TAuT	3.2	1.22	889	7.11	63.4	4.01
TAuT	3.2	1.34	897	6.18	66.3	3.67
TAuT	3.2	1.45	900	8.32	63.9	4.79
TAuT	3.2	2.29	873	10.82	68.5	6.47
TAuT	3.2	2.51	870	9.68	70.6	5.95
TAuT	3.2	2.73	887	11.86	67.4	7.09
TAuT	3.2	2.90	879	11.97	61.9	6.51
TAuT	3.2	4.01	853	11.74	63.9	6.40
TAuT	3.2	5.02	862	12.67	69.5	7.59
TAuT	3.2	5.81	856	13.57	69.8	8.10
TAuT	3.2	5.94	833	14.71	68.0	8.34
TAuT	3.2	8.80	832	14.94	73.2	9.10
TAuT	3.2	10.32	814	15.86	64.1	8.28
TAuT	3.2	10.58	811	19.15	60.6	9.41
TAuT	3.2	11.04	823	18.03	72.8	10.81
TAuT	3.2	11.71	814	18.13	61.6	9.08
TAuT	3.2	13.50	799	16.87	75.4	10.16
TAuT	3.2	13.84	808	17.82	70.4	10.13

Supplementary references

1. Hagfeldt, A.; Boschloo, G.; Sun, L.; Kloo, L.; Pettersson, H. *Chem. Rev.* **2010,** 110, (11), 6595-6663.
2. Xu, H. *Phys. Rev. B* **2005,** 72, (7), 073405.
3. Tanabe, K. *J. Phys. Chem. C* **2008,** 112, (40), 15721-15728.
4. Hu, M.; Chen, J.; Li, Z.-Y.; Au, L.; Hartland, G. V.; Li, X.; Marquez, M.; Xia, Y. *Chem. Soc. Rev.* **2006,** 35, (11), 1084-1094.
5. Millstone, J. E.; Hurst, S. J.; Métraux, G. S.; Cutler, J. I.; Mirkin, C. A. *Small* **2009,** 5, (6), 646-664.
6. Takai, A.; Kamat, P. V. *ACS Nano* **2011,** 5, (9), 7369-7376.
7. Choi, H.; Chen, W. T.; Kamat, P. V. *ACS Nano* **2012,** 6, (5), 4418-4427.
8. Qi, J.; Dang, X.; Hammond, P. T.; Belcher, A. M. *ACS Nano* **2011,** 5, (9), 7108-7116.
9. Ito, S.; Murakami, T. N.; Comte, P.; Liska, P.; Grätzel, C.; Nazeeruddin, M. K.; Grätzel, M. *Thin Solid Films* **2008,** 516, (14), 4613-4619.
10. Spuch-Calvar, M.; Pérez-Juste, J.; Liz-Marzán, L. M. *J. Colloid Interface Sci.* **2007,** 310, (1), 297-301.
11. Jones, M. R.; Osberg, K. D.; Macfarlane, R. J.; Langille, M. R.; Mirkin, C. A. *Chem. Rev.* **2011,** 111, (6), 3736-3827.
12. Cortie, M. B.; McDonagh, A. M. *Chem. Rev.* **2011,** 111, (6), 3713-3735.
13. Daniel, M.-C.; Astruc, D. *Chem. Rev.* **2003,** 104, (1), 293-346.
14. Skrabalak, S. E.; Au, L.; Li, X.; Xia, Y. *Nat. Protoc.* **2007,** 2, (9), 2182-2190.
15. Rycenga, M.; Cobley, C. M.; Zeng, J.; Li, W.; Moran, C. H.; Zhang, Q.; Qin, D.; Xia, Y. *Chem. Rev.* **2011,** 111, (6), 3669-3712.
16. *FDTD Solutions Reference Guide*. Lumerical Solutions: 2011.
17. Palik, E. D., *Handbook of Optical Constants of Solids*. Elsevier: 1998.
18. Kim, S. Y. *Appl. Opt.* **1996,** 35, (34), 6703-6707.
19. Bisquert, J.; Garcia-Belmonte, G.; Fabregat-Santiago, F.; Ferriols, N. S.; Bogdanoff, P.; Pereira, E. C. *J. Phys. Chem. B* **2000,** 104, (10), 2287-2298.
20. Halme, J.; Vahermaa, P.; Miettunen, K.; Lund, P. *Adv. Mater.* **2010,** 22, (35), E210-E234.
21. Bisquert, J.; Fabregat-Santiago, F.; Mora-Seró, I. n.; Garcia-Belmonte, G.; Giménez, S. *J. Phys. Chem. C* **2009,** 113, (40), 17278-17290.
22. Wang, M.; Chen, P.; Humphry-Baker, R.; Zakeeruddin, S. M.; Grätzel, M. *ChemPhysChem* **2009,** 10, (1), 290-299.
23. Wang, Q.; Ito, S.; Grätzel, M.; Fabregat-Santiago, F.; Mora-Seró, I.; Bisquert, J.; Bessho, T.; Imai, H. *J. Phys. Chem. B* **2006,** 110, (50), 25210-25221.